Joint Centre for Mesoscale Meteorology, Reading, UK

Variation of frontal structure along a cold front

K. A. Browning
N. M. Roberts

Internal Report No. 55

November 1995

Met Office Joint Centre for Mesoscale Meteorology Department of Meteorology
University of Reading PO Box 243 Reading RG6 6BB United Kingdom
Tel: +44 (0)118 931 8425 Fax: +44 (0)118 931 8791
www.metoffice.com

Designed and produced by the Met Office © Crown copyright 2001 01/0240 The Met Office logo is a registered trademark.

Version dated November 1995

Variation of frontal structure along a cold front

K A Browning* and N M Roberts

Joint Centre for Mesoscale Meteorology, University of Reading UK

Summary

A diagnostic study is presented to illustrate the process whereby a warm-conveyor-belt flow (WCB) is drawn into the circulation of a developing extratropical cyclone and interacts with dry air aloft to produce distinctive precipitation structures. The poleward boundary of part of the WCB was associated with a classical (ana-) cold frontal structure. The other part of the WCB flow, closer to the cyclone centre, was overrun by a 'dry intrusion' of low-θ_w air to give a split (kata-) cold front. The orientation of the surface cold front (ie the WCB boundary) changed significantly between these two parts but the orientation of the surface geostrophic flow within the WCB changed relatively little between the two parts. The surface cold front was characterised in most places by a narrow cold frontal rainband (NCFR) composed of shallow line convection elements (precipitation cores) aligned nearly parallel to the surface geostrophic flow in the WCB. The changing relationship between the frontal orientation and the direction of the surface flow accounts for the fact that the line convection elements occurred end-to-end to give almost 2-d line convection along the classical ana part of the cold front, but were non-aligned and widely spaced along the split cold front part.

***Corresponding address: Joint Centre for Mesoscale Meteorology, Harry Pitt Building, University of Reading, Whiteknights Road, PO Box 240, Reading RG6 6FN, UK.** **(The Joint Centre for Mesoscale Meteorology is supported by the Meteorological Office and the Department of Meteorology, University of Reading).**

1. Introduction

It has been argued on the basis of studies in the UK (Browning 1990) that a simple dual classification scheme developed from the idea of ana- and kata-cold fronts (Bergeron 1937) is a useful practical basis for analysing cold fronts. In the ana case, so-called warm-conveyor-belt (WCB) air with relatively high wet-bulb potential temperature (θ_w) rises in a region of rearward-sloping ascent above and behind the surface cold front (SCF) (Fig 1(a)). In the kata case the WCB air rises in a region of forward-sloping ascent ahead of the SCF (Figure 1(b)). The former (ana) fronts are generally regarded as the classical cold fronts. The latter (kata) fronts are sometimes referred to as split cold fronts (Browning and Monk 1982). Split cold fronts are characterised by dry air of relatively low θ_w (called a 'dry intrusion') overrunning the WCB ahead of the SCF. The leading edge of the dry intrusion, referred to as the upper cold front (UCF), triggers a band of precipitation ahead of and sometimes clearly separate from the SCF. Locatelli et al (1995), studying similar phenomena in the United States in the lee of the Rockies, refer to the UCF as a cold front aloft (CFA).

We shall use the terms classical and split cold fronts rather than ana- and kata-cold fronts in this paper. In our experience these fronts can change from one to the other either in space or in time. A common situation is for the cold front to be a split front just south of the centre of a developing cyclone and classical farther away where the cold front becomes a trailing feature. A case study of one such situation (8 December 1994), using routinely available observations in the UK and operational Limited Area and Mesoscale Model products from the Meteorological Office, forms the basis of the present paper.

Split cold fronts are often weakly-defined in terms of dry-bulb potential temperature (θ) but better-defined in terms of θ_w owing to a marked decrease in humidity. Although θ_w-fronts are not necessarily fronts in a dynamical sense, such θ_w-fronts do tend to be associated with the main cold frontal precipitation bands. We shall use the θ_w-fronts as our definition of cold fronts. In some respects, split cold fronts resemble warm occlusions; for example, in both cases relatively dry low-θ_w air overruns the surface front. However, in an idealized occlusion (Fig 1(c)) the high-θ_w air is absent from the layer close to the ground, whereas in a split cold front such as the one to be described in this paper, a belt of relatively high-θ_w air ('shallow moist zone') remains at low levels between the surface warm and cold fronts (Fig 1(b)).

A preview of the case study is provided by Fig 2 which depicts forecasts of θ_w-fronts at two times during the passage of the frontal system over the UK. The diagrams, showing the positions of the surface fronts and of the fronts at 600 mb, have been derived objectively using a code described by Hewson (1995). Hewson is deriving this kind of output routinely once a day from the 00 UTC forecast run of the 49-km grid Limited Area Model. Although the frontal positions differ slightly from those in the more up-to-date (06 UTC) runs used later in this paper, Fig 2 nevertheless indicates the essential features quite well. Air with relatively high θ_w extends northwards as a belt (WCB) which is 200 km wide at the surface and at 600 mb (and at intervening levels); but, as befits a split cold front, the rear edge of the belt of high-θ_w air is located substantially farther ahead at 600 mb than at the surface. The exception to this behaviour in Fig 2 is to the south of England at 09 UTC where the trailing cold front acquired a classical ana-frontal structure, the upper-level θ_w-front being situated poleward of

the SCF and analysed as a warm θ_w-front (ie an incipient cold frontal wave which, in the event, did not develop to the extent shown in Fig 2).

The structure of the paper is as follows. In Section 2 we demonstrate the coexistence of the two kinds of cold frontal structure - classical and split - along different parts of a single front. We especially concentrate on the development of the split portion and the overrunning dry intrusion. Then, in Section 3, we analyse the fine-scale structure of the narrow cold frontal rainband (NCFR) that occurred at the SCF along most of its length. In the split part of the cold front the NCFR consisted of highly-segmented, elongated, precipitation cores, corresponding to the shallow (<3km) line convection elements described by James and Browning (1979) and Hobbs and Biswas (1979). In the trailing part of the cold front, where it transformed to the classical structure, the line elements within the NCFR were aligned more nearly end-to-end. Although a detailed physical explanation is not given, the transition between the almost 2-dimensional line convection and the highly-segmented line elements is shown to be related to aspects of the larger-scale flow pattern described in Section 2.

2. Structure and evolution of the overall frontal system

(a) The tongue of high-θ_w air approaching the cyclone centre

The frontal system in this study was associated with a developing cyclone that crossed the British Isles on 8 December 1994. The evolution of the cyclone from 0 to 12 UTC is broadly indicated in Figure 3 which shows a sequence of infrared satellite images, with sea-

level pressure analyses superimposed, together with the 900-mb θ_w = 9°C isopleth. These diagrams draw attention to two features which are central to the later analysis:

- The tongue of high-θ_w air associated with the WCB which was being pulled out towards the cyclone centre (L) as it developed. This was part of a flow responsible for the large cloud-head pattern seen emerging northwards from the original polar-front cloud band situated over and to the south of the British Isles. An emerging cloud head is a well-known symptom of cyclogenesis (Evans et al 1994).

- The dry intrusion, close to and just south of the cyclone centre, which overran the tongue of high-θ_w air and produced a clearance of middle- and upper-level cloud above it (so-called dry slot). The dry intrusion and the general development of the cyclone were associated with a tropopause fold (see later), with values of potential vorticity of 2 PV units, indicative of stratospheric air, penetrating down to 5.5 km at location V.

Figure 4 shows a detailed analysis of surface observations depicting the high-θ_w tongue over the UK at 06 UTC, and Figure 5 shows the evolution of the high-θ_w tongue from 06 to 12 UTC as derived from the 06 UTC operational forecast run of the 17-km grid mesoscale model. Figures 4 and 5 reinforce the view that the tongue of warm air near the surface was being drawn out as a narrowing filament towards the cyclone centre. The fact that θ_w decreased northwards along the axis of the tongue might give the impression that the warm air was being occluded as it progressed northwards. There might have been some such effect owing to ascent of the warm air but an alternative way of interpreting the northward decrease

of θ_w is that it is merely a symptom of how far air with a pre-existing along-filament θ_w-gradient had penetrated northwards near the surface , ie almost the opposite of occlusion. Indeed there is even evidence in the model of seclusion of some high-θ_w air close to the surface near the cyclone centre at 12 UTC (eg Figure 5(c)).

(b) The dry intrusion and its effect on the rainfall pattern

Figure 6, showing the evolving pattern of relative humidity at 600 mb obtained from the 06 UTC forecast run of the mesoscale model, draws attention to the dry intrusion that was overrunning the SCF from the west. This corresponds to the dry slot seen in both the infrared imagery (Figure 3) and the water vapour imagery (not shown). The leading edge of the dry intrusion, shown later (Figure 14) to be associated with the leading edge of the θ_w-decrease, is depicted in Figure 6 as an UCF. The analysed position of the UCF corresponds to the mesoscale model's 95% relative humidity contour at the later time in Figure 6. However, the correspondence is not as good at 06 UTC (Fig 6(a)). The main evidence for the analysed position of the UCF at this time comes from the rainfall pattern, as explained shortly. The mesoscale model's underestimate of overrunning dry air at 06 UTC may be due to the availability of insufficient observations as the frontal system approached from the Atlantic or to deficiencies in the physical parametrizations, notably the convection scheme.

The weather radar data in Figure 7 can be interpreted in terms of three regimes of rainfall associated with the frontal system: a wide rainband at the leading edge of the system (extending all the way from northwest France to Scotland), a narrow cold frontal rainband (extending along the SCF from west of southwest England through Wales, to the coast of

northwest England), and a drier region in between which is punctuated by outbreaks of showers especially over central England. This is a similar arrangement of rainfall patterns to that analysed by Browning and Golding (1995) in which a wide band of uniform rain at the leading edge was separated from the narrow rainband along the SCF by a relatively dry, albeit convection-prone, zone due to an overrunning dry intrusion. We shall be discussing the narrow cold frontal rainband in detail in Section 3. Here we briefly focus on the wide rainband as an indicator of the position of the UCF. This rainband was a 200 km-wide belt of relatively continuous rain. Probably it was even more extensive than it appears because of the failure of some of the radars to detect precipitation at long range. Although there was embedded convection, the wide rainband is thought to have been due mainly to slantwise ascent of WCB air above the warm frontal zone. Its western boundary, which is seen to be ragged because of outbreaks of convection, is believed to have been associated with the arrival of the dry-intrusion air, marking the position of the UCF. The rear-edge of the wide rainband was typically 200 km ahead of the SCF. Locatelli et al (1989) present an example of a similar wide rainband associated with an UCF 300 km ahead of a SCF. The case they described differed from the present one in that the thrust of dry-intrusion air in their case overran the trailing *southern* part of the cold front and it was the portion of the cold front closer to the cyclone centre that had the classical rearward-sloping characteristics.

(c) Synthesis of the overall system

Figure 8 shows diagnostics for 06 UTC from the 00 UTC run of the Limited Area Model, to further clarify the 3-dimensional structure of the overall system. The 00 UTC Limited Area Model model run is used here because of the availability of the required

diagnostics even though there are some inconsistencies (mentioned shortly) with the later runs of the mesoscale model. The figure subdivides the system into a number of interlocking flows: Figures 8(a), (b) and (c) show system-relative flows in dry (a & b) or moist (c) isentropic surfaces and Figure 8(d) puts them together schematically.

Figures 8 (a) and (b) both depict the dry-intrusion flow. Figure 8(a) shows descending air at the base of the dry intrusion. It reached down to 1 km above msl just behind the SCF and we later demonstrate (Figures 16(c) and (17(b)) that some of it undercut the trailing part of the cold front, where it had the classical structure. Figure 8(b) shows air descending at a higher level within the dry intrusion before some of it overrides the SCF and reascends towards the UCF. This overall behaviour is consistent with the later runs of the mesoscale model except for a tendency (seen previously in Figure 2) for the dry intrusion to be too far advanced over southwest England and retarded over northern England (the analysed true position of the UCF is marked in Figures 8(a) and 8(b)).

Figure 8(c) shows moist air, emanating from the WCB, rising within an elongated cloud-head region, above the warm frontal zone (not explicitly labelled) and mainly ahead of the UCF. In Figure 8(d) the warm moist flow from Figure 8(c) is idealized as a warm conveyor belt, labelled W2: another flow of slightly warmer WCB air in the middle and upper troposphere, responsible for the original polar front cloud band, is idealized as the WCB-flow labelled W1. These WCB flows are put into a conceptual frame in Section 2(d). Note that, although the analysed position of the UCF in Figure 8(d) corresponds well with the clearance of the upper-level cloud along the coast of northeast England, over southern England the UCF

and the dry intrusion behind it extends into the region of high cloud; here the dry intrusion was hidden from the satellite by the veil of cirrus associated with W1.

The dry intrusion was closely associated with a tropopause fold. The vertical section, in Figure 9(a), shows dry-intrusion air with high potential vorticity (PV) emanating from near the fold. Values of PV in excess of 1 PV unit extend down to 600 mb and a tongue of air with relatively high PV and low humidity is seen sloping downwards along the isentropes towards the SCF. Figure 9(b), which depicts the relative flow within a surface between those in Figures 8(a) and 8(b), shows that the flow was largely parallel to the section in Figure 9(a). Most of the high-PV air within this section originated from high levels, although farther east over the UK at low levels (see Figure 9(b)) the high PV was being generated diabatically.

(d) The warm-conveyor-belt conceptualization

The WCB analysis in Figure 8(d) can be related to the concept of bifurcation of the WCB. This has been implicit in the literature for some time in the use of the labels W1 and W2 for two distinct WCB-flows (Young et al 1987, Browning and Roberts 1994, Young 1994). The W1/W2 convention has been used to denote a specific behaviour in a developing cyclone in which part (usually a leading edge) of the main WCB (W1) finds itself under the influence of a developing vortex and gets drawn out into a tongue of air (W2) which approaches the cyclone centre and ascends as a cloud head. A recent objective trajectory analysis by Wernli (1995) has clarified this process, leading to the conceptual model in Figure 10. The model shows three stages in the evolution of a bifurcating WCB in association with an upper-level vortex (V):

Time T+0 Elongated WCB

Time T+12h Showing leading part of WCB beginning to interact with the upper-level vortex. Mutual interaction between upper and lower levels pulls air parcels in part of the WCB (labelled W2) relatively northwestwards and induces the ascent within parts of it.

Time T+24h The above processes continue but, at the same time, the remaining part of the WCB (labelled W1) overruns the tail of W2 and turns anticyclonically in the upper ridge. The flow fanning-out within W2 forms the top part of the emerging cloud head of the developing cyclone. (The underlying part of the cloud head consists of cold-conveyor-belt (CCB) air not analysed here).

Sometimes (as in the early stages of the case study in the present paper, eg Figure 3(b)) the convex outward edge of the upper cloud band accompanying W1 is sharply defined in the satellite imagery where it crosses over W2. On other occasions (as in the later stages of the present case) the ascent along the shaft of the W2 arrow in Figure 10 is sufficient to generate cloud tops as high as those in the W1-flow, in which case the distinction between the two flows tends to disappear.

A variety of configurations can occur in this bifurcation process depending on the large-scale flow pattern in which it is embedded and, perhaps, on the size of the upper vortex, V, or how closely it approaches the original WCB. In some situations, for example, when there is a confluent upper trough, and if the vortex is small or its approach is close, the shaft of the W2 arrow may be correspondingly short and the resulting configuration as described

in Browning and Roberts (1994). In other situations, especially when there is a diffluent trough at 300 mb, the W2 flow may be longer, as depicted in Young's (1994) conceptual model (Figure 11). The case analysed in the present paper was associated with a weakly diffluent trough (not shown) and is, perhaps, closer to the model in Figure 11.

3. Mesoscale analysis of the frontal system

We have already described, in Section 2, the broad-scale structure of the cold frontal system, showing that its northern parts were characterised by a split cold-frontal type of structure due to an overrunning dry intrusion, and indicating that the southern parts were characterised instead by a classical cold-frontal structure. In this section we relate the structure of the precipitation distribution at the surface cold front to the frontal type, for which purpose we shall present rather more detailed evidence to justify our claim that different portions of the same front had distinctly different structures. We begin this section by describing the mesoscale structure of the NCFR in relation to the detailed sea-level pressure analysis along the length of the SCF to demonstrate the existence of two different NCFR structures (Section 3(a)). We then present cross-sections to show that the corresponding frontal structure changed from that of a split cold front in one part (Section 3(b)) to that of a classical cold front in the other (Section 3(c)). We then examine the evolution of elements within the NCFR as they travelled from one part of the front to the other (Section 3(d)). Finally in Section 3(e), we discuss possible mechanisms that might account for this evolution.

(a) Analysis of the surface cold front and narrow cold frontal rainband (NCFR)

The time 09 UTC has been chosen for detailed analysis because this was when the two contrasting parts of the SCF were both within range of the dense UK observational network. Figure 12(a) shows that the SCF at 09 UTC was defined by a pronounced trough, with an abrupt rise in sea-level pressure over much of central and southwest England but not farther north, towards the Wash. In Figure 12(b) the pressure analysis from Figure 12(a) is superimposed upon the rainfall pattern obtained from the weather radar network. It shows a well-defined NCFR along the pressure trough. Evidence from multiple elevation radar scans shows that the NCFR was shallow ($\leq$3 km). In the southern portion of the front, where we shall show it was a classical cold front, the NCFR was in the form of fairly 2-dimensional line convection. In the northern (split cold frontal) portion of the front, the line convection breaks up into line elements orientated almost parallel to the surface geostrophic flow just ahead of the SCF. There were widespread outbreaks of rain ahead of the NCFR in this region and farther south. Widespread light-to-moderate rain also extended behind the SCF in the southern part of the cold front owing to the slantwise ascent of mid-tropospheric air (see later Figure 16).

(b) Cross-section in the split cold frontal region

Figure 13 shows the frontal analysis at 09 UTC superimposed on the Meteosat water vapour imagery, (the corresponding infra red image was not available but the WV image enables us to make the required points). The split cold frontal region is the region where an UCF is analysed ahead of the SCF. The split structure is borne out by Figures 14 (a and b) which portray a vertical cross-section from the mesoscale model along the line K_1K_2 in Figure

13. The position of this section has been chosen so as to correspond to the general egion of highly-segmented NCFR line elements as shown in Figure 12(b).

The split cold front structure is evident in Figures 14(a and b) from the way in which dry-intrusion air, with low θ_w, extends some 150 km ahead of the SCF at levels between 800 and 600 mb. The leading edge of the dry intrusion is marked as an UCF and, ahead of it, WCB air, characterised here by $\theta_w > 10.5°C$, slopes forwards in the lower troposphere as described in Section 2(a). The overrunning aloft is evident in the mesoscale model's front-normal winds which are plotted in Figure 14(b) at the position of the SCF. The overrunning air includes both the dry-intrusion air (which originates from higher levels to the north and northwest) and a deck of moister upper-level air at which level the winds are parallel to the streaks of moist air and cirrus cloud seen in the imagery in Figure 13. Farther to the southwest in Figure 13 the orientation of these streaks can be seen to be backed, implying a rearward component of flow relative to the front. This is indicative of the classical cold frontal structure in the trailing part of the front, described next.

(c) Cross-section in the classical cold frontal region

We have chosen to illustrate the vertical structure of the classical cold frontal region at 11 UTC, two hours after the split-cold-frontal section just described, because of the availability of three well-located radiosondes at the later time. The position of the chosen cross-section X_1X_2, together with the locations of sondes at Aughton (A), Larkhill (L) and Herstmonceux (H), are plotted in Figures 15(a) and (b), superimposed on the corresponding Meteosat infrared image and radar network rainfall pattern, respectively. (Motion of the system was such that this section would correspond to one normal to the front through Devon

(D) at the earlier time corresponding to Figure 13.) The section X_1X_2 goes through the straight and relatively 2-dimensional part of the NCFR.

The NCFR, where it was crossed by X_1X_2, was embedded within a wider belt of moderate rain which occurred mostly ahead but also extended about 30 km behind. The rearward extent of this rain increased to the southwest of section X_1X_2 where there was an incipient frontal wave. The wave was associated with a suspected small closed low shown by a single ship observation at 3°W, 49.8°N, but the wave did not develop, nor did it cause the NCFR along the SCF to deviate from a straight line. (An interesting feature that we shall not pursue here is the almost west-east orientated arc of a narrow rainband which morphologically looked like an extension of the NCFR but instead is likely to have been at the leading edge of a pulse of slightly higher-θ_w air).

Returning to the section X_1X_2, the vertical structure in this region is shown in the multiple-part diagram in Figure 16. The first two parts, (a) and (b), are model-derived plots of relative humidity and θ_w, respectively. They are analyses for 12 UTC shifted according to the system velocity to correspond to a 11 UTC analysis for easy comparison with observations made at 11 UTC. The observations are represented in Figure 16(c) which has been derived manually from an analysis of radiosonde ascents (Figure 17), surface reports, satellite and radar imagery, all interpreted in the light of the (in some regards) degraded model-derived patterns. The classical cold frontal structure is unmistakable, with subsaturated low-θ_w air undercutting rearward-sloping ascent of high-θ_w air which has originated from the WCB ahead of the SCF. (From a model perspective it is interesting to note that the mesoscale model failed to simulate the true sharpness of the front at low levels; indeed other

output (not shown) indicates that it failed to reporduce the strong vorticity and heavy rain at the SCF. This may be due to shortcomings in the parametrization of convection, as noted earlier).

(d) Evolution of the structure of the narrow cold frontal rainband (NCFR)

The previous analysis has shown that the cold front changed from being a classical cold front in its southwestern part to a split cold front in its northeastern part. At 06 UTC the transition probably occurred just west of Cornwall. The radar data for 06 UTC in Figure 7 show that, towards the classical part, the NCFR was a rather straight feature, orientated southwest-northeast. However, in the split part, over Wales, it curved away in a more south-north direction, and the associated echo pattern became more broken. A clearer picture of this transition is obtained at the later time of 09 UTC analysed in detail in Section 3(a), when the transition occurred over central southern England, in the centre of the dense observing network. Figure 18(a) shows the composite radar picture for 0930 UTC at 5 km resolution and Figure 18(b) shows the echo pattern from a single radar at 2 km resolution for part of the NCFR.

An analysis of a series of pictures like that in Figure 18(a) is reproduced in Figure 19. For simplicity this depicts individual radar echoes within the NCFR without regard to their intensity. In fact, the long, almost 2-dimensional echo feature in the southwestern part had intensities estimated to be generally in excess of 4 mm h^{-1} averaged over 5 km squares, whereas such intensities were attained only locally in parts of the precipitation cores farther north. When viewed at higher resolution, even the so-called 2-d portion had some cellular

sub-structure. Thus Figure 18(b) shows cores of 8 mm h^{-1} intensity, typically 2 km wide and 10 km long, embedded within the otherwise rather 2-d line of heavy precipitation. However, the along-front modulation of intensity in Figure 18(b) is seen to be relatively weak. Moreover, these precipitation cores are orientated parallel to the overall line convection and, except in one place, they are aligned more or less end-to-end. Bearing in mind the possible topographic disturbances in the low-level flow converging towards the SCF, the line convection here is remarkably close to 2-dimensional.

Successive NCFR patterns are depicted in Figure 19 at hourly intervals. Precipitation cores can be tracked for up to 4 hours travelling at 125 ± 15 km h^{-1} (35 ± 4 m s^{-1}) from 248 ± 4 deg, as shown by the arrows. Individual precipitation cores can be seen breaking away from the 2-d part of the line after they enter the region where the orientation of the SCF (thin lines) turns northward at a significant angle to the preferred orientation of the line elements. Although it is difficult to specify precisely the point where the cold front changes from classical to split, the point where the orientation of the SCF begins to change (the turning point) does appear approximately to mark the transition from the classical to split part. As the line elements travelled from the classical part to the split part, it is seen that their orientation may have changed a little but such changes were small compared with the change in the overall orientation of the SCF itself.

(e) Possible mechanisms for the transition from 2-d line convection to highly segmented line elements

One of the most frequently quoted mechanisms for explaining the generation of segmented line-convection is the breakdown of the horizontal shear at the SCF. Ahead of the SCF in the present case there was a low-level jet parallel to the front, with maximum winds of 35 ms^{-1} at 900 mb (see Herstmonceux sounding in Figure 17(c)). The front-parallel wind component at this level dropped to half this speed just behind the SCF (see Larkhill sounding in Figure 17(b)). We have no direct observations, apart from the abruptness of the surface transition (Figure 12), to prove that the cyclonic shear associated with the decrease in this wind component was concentrated at the line convection, but observations in similar fronts (eg Browning and Harrold (1970), Carbone (1982), Bond and Fleagle (1985)) suggest that the transition probably was sharp over the depth of the line convection, at least across the intense precipitation cores. Matejka (1980) (see also Hobbs and Persson 1982) propose a specific process whereby shearing instabilities in such a situation create perturbations along an initially 2-dimensional length of line convection, and these then amplify to become line elements reorientated at an angle to the original line (Figure 20). Such reorientation is not supported by our observations which, as summarized in Figure 21, show that, instead, the line elements to a first approximation retain their original orientation as they move into a region where the orientation of the SCF is changing under the influence of larger-scale dynamical forcing. It seems that in this case the change to broken line elements is due to the changing orientation of the part of the SCF in which they find themselves rather than to a change in the orientation of the line elements as in the shearing instability theory.

The segmented line elements in this study had many similarities to the wavelike rainbands observed in detail by Wang and Hobbs (1983). The rainbands they studied were situated close to a surface cold front and they had the following properties: top to 2-3 km,

width 3-5 km, length 80 km, spacing 5-10 km, rainfall intensity up to 3 mm h^{-1} , orientation parallel to the winds in the upper parts of the rainband, lapse rate slightly unstable. They showed that their properties were consistent with horizontal roll vortices in the boundary layer reinforced by latent heat effects. The underlying mechanism was attributed to inflection-point instability in the boundary layer (eg Brown 1980). To the extent that our line elements were parallel to the surface geostrophic flow and had other properties similar to those listed above, a similar mechanism might apply in the present case. It is, however, not clear that the wavelike rainbands they observed were in all respects identical to the line elements in the present study. For example, although their wavelike rainbands appeared to coexist with line convection in neighbouring parts of the SCF, the orientation of the wavelike rainbands differed considerably from that of elements within the line convection. Another difference is that the rainfall intensity in our line elements was more intense. Since the above boundary-layer instability theories tend to assume a horizontally homogeneous basic flow without precipitation processes, we must look elsewhere for a complete explanation.

A mechanism for organizing shallow convection in which precipitation plays an active part has been proposed by Miller (1978). In his mechanism precipitation induces downdraughts which tend to cause a line of convection to become orientated parallel to an appropriate vertical wind shear vector. According to Miller, the wind-shear vector between the motion of a convective cell and the outflow at the top of its updraught determines the direction in which precipitation falls out. This then generates a line of new updraughts via the effects of precipitation-induced downdraughts. In the present case the wind shear between mid-cloud level (800 mb) and the top of the line convection cloud at 700 mb (not shown) was orientated roughly in the direction of the observed line elements; however, because of the

small magnitude of the wind change over such a small height interval, it is unclear how the mechanism suggested by Miller could have been effective in this case for precipitation cells which, with such low tops, provided little opportunity for precipitation to be carried a long way downshear. Individual precipitation cores were typically 50 km long but even those precipitation particles falling as slowly as, say, 3 m s^{-1} in a relative outflow averaging 10 m s^{-1}, would have drifted only 10 km downshear while falling to the ground over a period of 20 minutes.

We are thus left without a well-defined theoretical explanation for the orientation of the line-convection elements. Small-scale numerical modelling studies based on realistic observational data, and with a model resolution capable of resolving the convection, are needed to address this issue. One such study (Dudhia 1993) using a 7 km-grid nonhydrostatic mesoscale model to simulate an Atlantic cold front, has succeeded in reproducing a realistic NCFR. The overall NCFR in Dudhia's study was orientated south-southwest - north-northeast and the low-level ascent within it occurred as a series of narrow bands orientated southwest - northeast. A sensitivity study revealed that removing surface friction caused the bands to be reorientated more nearly perpendicular to the cold front. According to Dudhia, this suggests that the orientation of the line elements is related to the relative direction of low-level inflow to the line convection, which is sensitive to friction.

4. Conclusions

The overall frontal configuration that we have described was established by the interaction of a low-level baroclinic zone with an upper-level potential-vorticity maximum and

tropopause fold. The latter was accompanied by a 'dry-intrusion' of low-θ_w air approaching from the northwest. In the northern part of the system, within several hundred kilometres of the cyclone centre, the dry intrusion overrode a narrowing tongue of relatively high-θ_w air and advanced ahead of the surface cold front to give a structure consistent with the split-cold-front model of a kata-cold front. Farther south, in the trailing part of the cold front, the dry low-θ_w air undercut rearward-ascending high-θ_w air to give a classical ana-cold front.

The transition between the split-front and classical-front parts of the cold front was marked by a change in the structure of the narrow cold frontal rainband (NCFR) that occurred along the surface front. Everywhere the narrow cold frontal rainband was due to a very narrow band of strong updraught, less than 3 km deep, ie line convection. However, there was a transition from almost continuous 2-dimensional line convection in the region of the classical cold front to distinctly broken line convection elements, oriented at 30° to the mean direction of the surface cold front, in the region of the split-cold front. Individual line elements originated at the northern end of the continuous line convection within the classical part of the front and advected into the split-cold-front part where they could be tracked as broken line elements for over 4 hours. This transition to broken line elements was due to a change in the orientation of the surface cold front with respect to the preferred orientation of the convective line elements: it was not due to a change in the orientation of the line elements themselves, because this remained essentially constant as they travelled from the classical part of the front to the split part. Thus the observed behaviour in this case is inconsistent with the mechanism proposed by Matejka (1980) in which shearing stabilities lead to the creation of strongly segmented elements of line convection by the reorientation of sections of an initially 2-dimensional strip of line convection.

The analysis in this paper has shown that the structure of an individual cold front can vary significantly in both space and time and that the 2-dimensional approach used in many theoretical studies of frontogenesis might not always be an appropriate idealization. Although the particular frontal configuration described is thought to be fairly common, at least in the UK, the detailed mix of ingredients does vary a lot from case to case. It is, for example, by no means clear that the transition in the structure of the narrow cold frontal rainband described here is necessarily always linked to a transition from classical to split cold frontal structure. Despite the many studies of narrow cold frontal rainbands that have been made in recent years there is still much to be learned about how their existence and detailed structure is determined by the particular combination of larger-scale forcing and boundary-layer processes. Because of the very heavy rain and occasionally damaging winds associated with narrow cold frontal rainbands, this is an important practical problem as well as an intriguing research topic requiring further attention.

Acknowledgements

The authors wish to thank Tim Hewson (at the Joint Centre for Mesoscale Meteorology) for providing the objective frontal analyses in Figure 2, and Heini Wernli (at the Swiss Federal Institute of Technology, Zürich) for providing the objectively identified airstream analyses that underpinned the conceptual model in Figure 10. We are also grateful to an anonymous referee whose constructive comments led us to present additional analyses to support our interpretations.

References

Bergeron, T., 1937 On the physics of fronts. *Bull.Amer.Meteorol.Soc.*, 18, 265-275.

Bond, N.A., and Fleagle, R.G., 1985 Structure of a cold front over the ocean. *Q.J.R.Meteorol.Soc.*, 111, 739-759.

Brown, R.A., 1980 Longitudinal instabilities and secondary flows in the planetary boundary layer: a review. *Rev.Geophys.Space Phys.*, 18, 683-697.

Browning, K.A., 1990 Organization of clouds and precipitation in extratropical cyclones. Pp 129-153 in *Extra-tropical cyclones: Erik Palmén Memorial Volume*. Eds C Newton and E O Holopainen, American Meteorological Society, Boston, Mass., 1990.

Browning, K.A., 1995 Mesoscale aspects of extratropical cyclones: an observational perspective, JCMM Internal Report 44, 60 pp.

Browning, K.A. and Golding, B.W., 1995 Mesoscale aspects of a dry intrusion within a vigorous cyclone, *Q.J.R.Meteorol.Soc.*, 121, 463-493.

Browning, K.A. and Harrold, T.W., 1970 Air motion and precipitation growth at a cold front. *Q.J.R.Meteorol.Soc.*, 96, 369-389.

Browning, K.A., and Monk, G.A. 1982 A simple model for the synoptic analysis of cold fronts. *Q.J.R.Meteorol.Soc.*, 108, 435-452.

Browning, K.A. and Roberts, N.M., 1994 Structure of a frontal cyclone, *Q.J.R.Meteorol.Soc.*, 120, 1535-1557.

Carbone, R.E., 1982 A severe frontal rainband. Part I: Stormwide hydrodynamic structure. *J.Atmos.Sci.*, 39, 258-279.

Dudhia, J., 1993 A non-hydrostatic version of the Penn State - NCAR Mesoscale Model: validation tests and simulation of an Atlantic cyclone and cold front, *Mon.Wea.Rev.* 121, 1493-1513.

Evans, M.S., Keyser, D., Bosart, L.F. and Lackmann, G.M., 1994 A satellite-derived classification scheme for rapid maritime cyclogenesis, *Mon.Wea.Rev.*, 122, 1381-1416.

Hewson, T.D., 1995 Objective Fronts. JCMM Internal Report.

Hobbs, P.V. and Biswas, K.R., 1979 The cellular structure of narrow cold-frontal rainbands. *Q.J.R.Meteorol.Soc.*, 105, 723-727.

Hobbs, P.V. and Persson, P.O.G.1982 The mesoscale and microscale structure and organization of clouds and precipitation in midlatitude cyclones. Part V: The substructure of narrow cold-frontal rainbands. *J.Atmos.Sci.*, 39, 280-295.

James, P.K. and Browning, K.A., 1979 Mesoscale structure of line convection at surface cold fronts, *Q.J.R.Meteorol.Soc.*, 105, 371-382.

Locatelli, J.D., Martin, J.E., Castle, J.A. and Hobbs, P.V., 1995 Structure and evolution of winter cyclones in the central United States and their effects on the distribution of precipitation. Part III: The development of a squall line associated with weak frontogenesis aloft. *Mon.Wea.Rev.*, 123, 2641-2662.

Locatelli, J.D., Sienkiewiez, J.M. and Hobbs, P.V., 1989 Organization and structure of clouds and precipitation on the Mid-Atlantic coast of the United States. Part I: Synoptic evolution of a frontal system from the Rockies to the Atlantic coast. *J.Atmos.Sci.*, 46, 1327-1348.

Matejka, T.J., 1980 Mesoscale organization of cloud processes in extratropical cyclones. PhD thesis, University of Washington, 361 pp.

Miller, M.J., 1978 The Hampstead storm: A numerical simulation of a quasi-stationary cumulonimbus system. *Q.J.R.Meteorol.Soc.*, 104, 413-427.

Young, M.V., 1994 A classification scheme for cyclone life-cycles: applications in analysis and short-period forecasting. In 'The life cycles of extratropical cyclones, Vol III, Proc.international symposium, 27 June - 1 July 1994, Bergen, pp 380-385.

Young, M.V., Monk, G.A. and Browning, K.A., 1987 Interpretation of satellite imagery of a rapidly deepening cyclone. *Q.J.R.Meteorol.Soc.*, 113, 1089-1115.

Wang, P-Y., and Hobbs, P.V., 1983 The mesoscale and microscale structure and organization of clouds and precipitation in midlatitude cyclones. X: Wavelike rainbands in an occlusion, *J.Atmos.Sci.*, 40, 1950-1964.

Wernli, J.M., 1995: Lagrangian perspective of extratropical cyclogenesis, PhD Dissertation No 11016, Swiss Federal Inst of Tech, Zürich, 157 pp.

Figure Legends

Figure 1 Simple idealizations of (a) an classical (ana)-cold front, (b) a kata-cold front fitting the split-front model, and (c) a warm occlusion. Different parts of the cold front in the present case study are analysed in terms of (a) and (b). The arrows indicate that (a) and (b), respectively, fit the descriptions of a warm conveyor belt with (a) rearward-sloping ascent and (b) forward-sloping ascent. Note that the cold (C) and warm (W) air masses and frontal boundaries between them are identified here in terms of wet-bulb potential temperature (θ_w). The dry-bulb (θ) fronts tend to be situated farther into the cold θ_w airmasses, especially aloft when the airmass is very dry as might be the case in the cold frontal zones in (b) and (c).

Figure 2 Objective diagnoses of θ_w-fronts (wet-bulb potential temperature fronts), defined as the high-θ_w side of zones across which the magnitude of the θ_w-gradient is changing most steeply, at (a) 06 and (b) 09 UTC, 8 December 1994, obtained from the 00 UTC run of the operational Limited Area Model. Surface fronts: black lines with solid symbols. Upper (600 mb) fronts: grey lines with open symbols. Sea-level pressure is also shown. (Courtesy of Tim Hewson, JCMM).

Figure 3 Sequence of Meteosat infrared images at (a) 00, (b) 03, (c) 06 and (d) 12 UTC, 8 December 1994, showing a cloud head emerging to the north of a polar front cloud band (labelled in (b)), with an expanding dry slot forming between them. Grey shades denote brightness temperatures as follows: white <-44°C, light grey <-32°C, medium grey <-20°C, dark grey <-8°C, very dark grey $\geq$-8°C. The images in (a), (c) and (d) are superimposed on the sea-level pressure analyses (mb) as derived from the 00 UTC run of the operational Limited Area Model. Also shown is the 9°C contour of wet-bulb potential temperature at 900 mb, depicting a tongue of warm moist air being drawn out as a filament into the circulation of the developing low, centred at L. V shows the central position at 5.5 km of an upper vortex associated with a tropopause fold that was feeding upper-level (dry-intrusion) air into the dry slot.

Figure 4 Analysis of surface wet-bulb potential temperature (°C) at 06 UTC, 8 December 1994, derived from synoptic stations plus a few autographic records converted from time to space according to the system velocity. Autographic data show up as regular lines of plotted numbers. Observations based upon reports at adjacent hours are plotted in brackets. Dots after numbers denote ½.

Figure 5 Warm moist tongue at 950 mb at (a) 06, (b) 09 and (c) 12 UTC, 8 December 1994, derived from the 06 UTC forecast run of the operational mesoscale model. Isopleths are of wet-bulb potential temperature (θ_w) at 1°C intervals above 9°C. The centre of the low is at L. The surface cold front is drawn solid black where it is based on detailed radar and surface observations; elsewhere it is drawn grey. The dashed frame shown in (a) depicts the area of Figure 4.

Figure 6 Dry intrusion at 600 mb at (a) 06, (b) 09 and (c) 12 UTC, 8 December 1994, derived from the 06 UTC forecast run of the operational mesoscale model. Isopleths are shown for 95 and 50% relative humidity. The surface cold front is shown as in Figure 5. The analysed position of the upper cold θ_w-front (wet-bulb potential temperature front) is depicted with open symbols.

Figure 7 Radar rainfall pattern for 06 UTC, 8 December 1994, superimposed on Meteosat infra-red imagery. Colours represent rainfall rates averaged over 5 km squares approximately as follows: red > 6, yellow > 4, green > 2 and blue > 0.5 mm h^{-1}. Also shown is the maximum coverage of the radar network, if the precipitation were deep enough to be detected. The diagonal hatching is the authors' assessment of likely areas of widespread rain not detected because of its long range from individual radars in the radar network. Grey shades denote brightness temperatures as follows: white <-40°C, light grey <-20°C, medium grey <0°C, dark grey $\geq$0°C.

Figure 8 Aspects of the three dimensional flow pattern associated with the frontal system at 06 UTC, 8 December 1994, derived from the 00 UTC forecast run of the operational Limited Area Model. (a) and (b) depict the dry intrusion, (c) depicts part of the warm moist flow, and (d) synthesises these features within the context of satellite cloud imagery. In more detail (a) shows the height of, and the relative humidity and system-relative flow within, the θ = 15°C isentropic surface. Also shown are the analysed positions of the surface cold front and upper cold θ_w-front. (b) is similar to (a) but for the θ = 25°C isentropic surface. (c) shows the height of the θ_w = 10°C moist isentropic surface, plus the system-relative flow in this surface where the warm air is above the frictionally retarded lowest kilometre. The area with relative humidity exceeding 95% is shaded. (d) shows the flow pattern from (a) (dashed lines) and the flow pattern from (b) (solid lines) superimposed on the frontal analysis and the Meteosat infrared image (grey scales as in Figure 3(c)). Also shown in (d) are the warm conveyor belts W2 (based on (c)) and W1 (detailed analysis not shown).

Figure 9(a) Cross-section along AB in Figure 9(b), drawing attention to aspects of the tropopause fold at 06 UTC, 8 December 1994, derived from the same model runs as Figure 8. Solid curves are potential vorticity labelled in PV units with increasingly dark shading for PV > 0.5, 1.0, 1.5 and 2.0 PVU. The thick curve shows the downward protrusion of air with relative humidity less than 50%. Dashed curves show isentropes for θ = 15°C (corresponding to Figure 8(a)), θ = 20°C (corresponding to Figure 9(b)) and θ = 25°C (corresponding to Figure 8(b)).

Figure 9(b) Distribution of potential vorticity and system-relative flow within the θ = 20°C isentropic surface at 06 UTC, 8 December 1994, derived from the same model run as Figure 8 and showing the location of the section in Figure 9(a). Solid curves show potential vorticity with shading as in Figure 9(a). Height of the isentropic surface is shown by dashed curves at 2, 3, 4 and 5km.

Figure 10 Conceptual model of a warm conveyor belt (WCB) bifurcating into flows W1 and W2 (open arrows) in association with an upper-level potential-vorticity maximum (centred at V) approaching the WCB. (Adapted from Browning 1995, and building on Wernli 1995).

Figure 11 Conceptual model showing system-relative airflows associated with Young's diffluent-flow type of cyclogenesis. The arrows labelled W1 and W2 are warm conveyor belts. The dashed arrow, labelled CCB (not discussed in the text) is a cold conveyor belt. (After Young 1994).

Figure 12 Detailed sea-level pressure analysis for 09 UTC, 8 December 1994, with isobars (mb) superimposed on station observations (last 2 figures only) and surface cold front in (a) and radar rainfall pattern in (b). Grey shades in (b) represent rainfall rates exceeding approximately 0.5, 1, 2 and 4 mm h^{-1} averaged over 5 km squares.

Figure 13 Analysed positions of the surface cold front and upper cold θ_w-front at 09 UTC, 8 December 1994, superimposed on the Meteosat water vapour image for 0930 UTC adjusted to correspond to 09 position. Dark areas correspond to dry air; light areas to moist air and cloud. The dashed frame shows the area depicted in Figure 12. K_1K_2 marks the position of the section in Figure 14. D marks the location of Devon, referred to in the text.

Figure 14 Cross-section along K_1K_2 in Figure 13 for 09 UTC, 8 December 1994, derived from the 06 UTC forecast run of the operational mesoscale model. (a) shows relative humidity, with contours at intervals of 5% (shaded where RH < 90%). (b) shows wet-bulb potential temperature with contours at 0.5°C intervals. Wind arrows above the surface cold front show model-derived relative wind components normal to the SCF.

Figure 15 (a) Analysed position of the surface cold front at 11 UTC, 8 December 1994, superimposed on the corresponding Meteosat infrared image and (b) the radar network picture for the same time (grey shades represent rainfall rates exceeding approximately 0.5, 1, 2 and 4 mm h^{-1}). Also shown are the location X_1X_2 of the section in Figure 16 and the locations of the radiosonde ascents at Aughton (A), Larkhill (L) and Herstmonceux (H), shown in Figure 17.

Figure 16 (a, b, c) Cross-section, along X_1X_2 in Figure 15 for 11 UTC, 8 December 1994: (a) mesoscale model-derived relative humidity (contours at intervals of 5%; shaded where RH < 90%, (b) mesoscale model-derived wet-bulb potential temperature (contours at 0.5°C intervals; θ_w = 8 and 11°C shown bold), (c) composite diagram derived from observations alone: dashed contours show θ_w = 8 and 11°C derived from radiosondes A, L and H; thin horizontal arrows show front-normal wind components relative to front derived from the same 3 radiosondes; vertical hatching denotes surface rainfall with spacing proportional to rainfall intensity; columnar feature above the heaviest rain is line convection as observed by radar; cusped line at top of diagram represents the cloud top as inferred from infrared imagery (cloud top height is probably

underestimated where emissivity is thought to be low); thin curve represents cloud base inferred from surface observations; circles and semicircles show individual observations of total and partial cloud cover, respectively; bold arrows show schematic ana-cold frontal circulation.

Figure 17 Temperature and dewpoint curves plotted on tephigrams, plus wind soundings, for (a) Aughton (A), (b) Larkhill (L) and (c) Herstmonceux (H) at 11 UTC, 8 December 1994. These soundings were used in the derivation of Figure 16(c). Their locations are plotted in Figure 15.

Figure 18 (a) Part of a radar network picture at 0930 UTC, 8 December 1994, showing the precipitation distribution at 5 km resolution. Grey shades represent rainfall rates exceeding approximately 0.5, 1, 2 and 4 mm h^{-1} averaged over 5 km squares. The circle, centred at the Warden Hill radar, shows the area of Figure 18(b).

(b) Rainfall pattern from a single radar at Warden Hill, showing part of (a) at 2 km resolution out to 75 km range. Grey shades represent rainfall rates exceeding approximately 4, 8 and 16 mm h^{-1} averaged over 2 km squares.

Figure 19 Analysis of the precipitation cores (line elements) along the narrow cold frontal rainband (NCFR) at 0530, 0630, 0730, 0830 and 0930 UTC, 8 December 1994. Alternate times are shaded in contrasting style.

Figure 20 Matejka's mechanism for the creation of strongly segmented line convection elements from an initially two-dimensional strip of line convection at a surface cold front. The diagram shows the hypothesized flow of air at low levels in a frame of reference moving with a cold front that develops a wavelike distortion. Shaded arrows represent the horizontal flow of air near the surface in the low-level jet ahead of the cold front. This air undergoes convergence at the cold front, where it ascends in a narrow updraught. Open arrows represent the horizontal flow of air immediately behind the cold front. (a) Initially uniform frontal wind shift line. (b) A perturbation is introduced on the front. (c) The perturbation amplifies, producing small lines of enhanced horizontal convergence (dashed lines) between which are zones of suppressed convergence. (Adapted from Matejka, 1980 by Hobbs and Persson, 1982. Reprinted with permission from the American Meteorological Society.)

Figure 21 Idealized representation of the line convection elements within the narrow cold frontal rainband in the present case study, showing how aligned elements within the southern (classical) part of the cold front successively cross over into the northern (split) part of the front and become non-aligned. The dashed line shows the track of the 'turning point' in the surface cold front to the north of which its orientation begins to turn more towards the north.

Figure 1

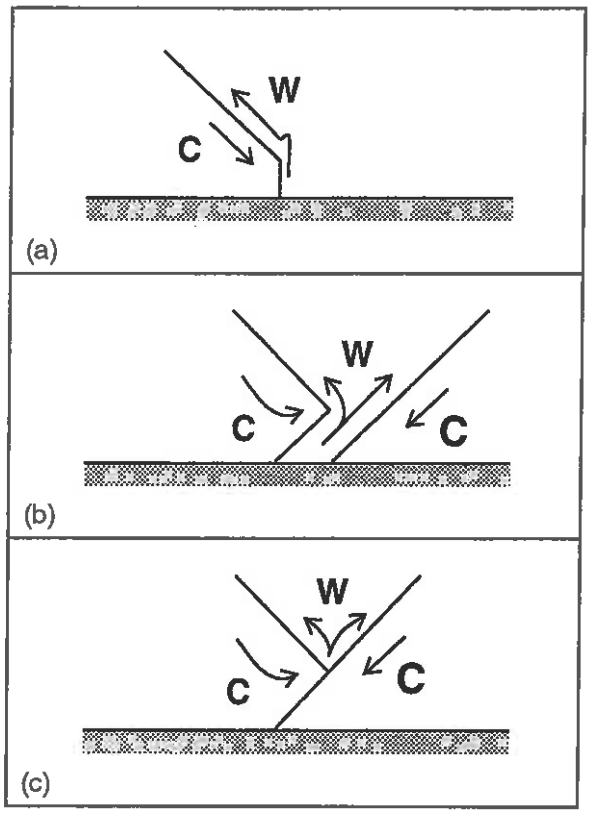

Figure 2

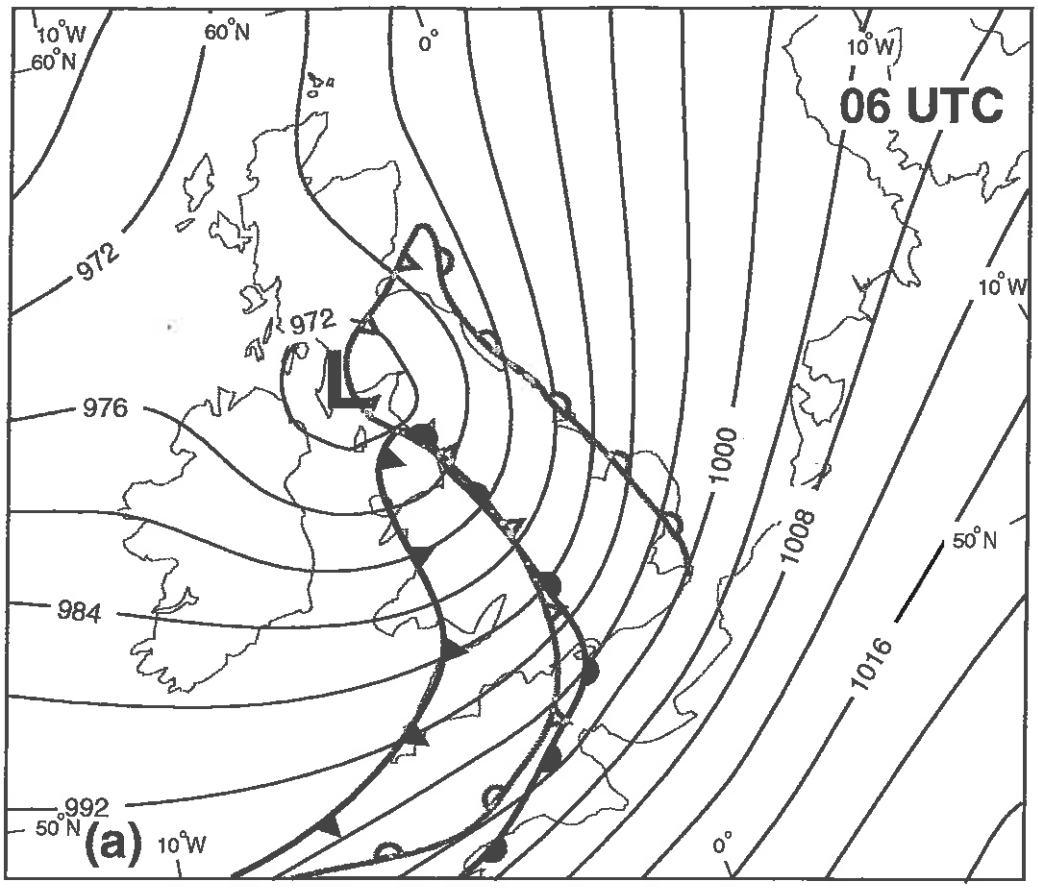
10°W
60°N
60°N
0°
10°W
06 UTC
10°W
972
L
976
1000
1008
50°N
984
1016
992
50°N
(a)
10°W
0°

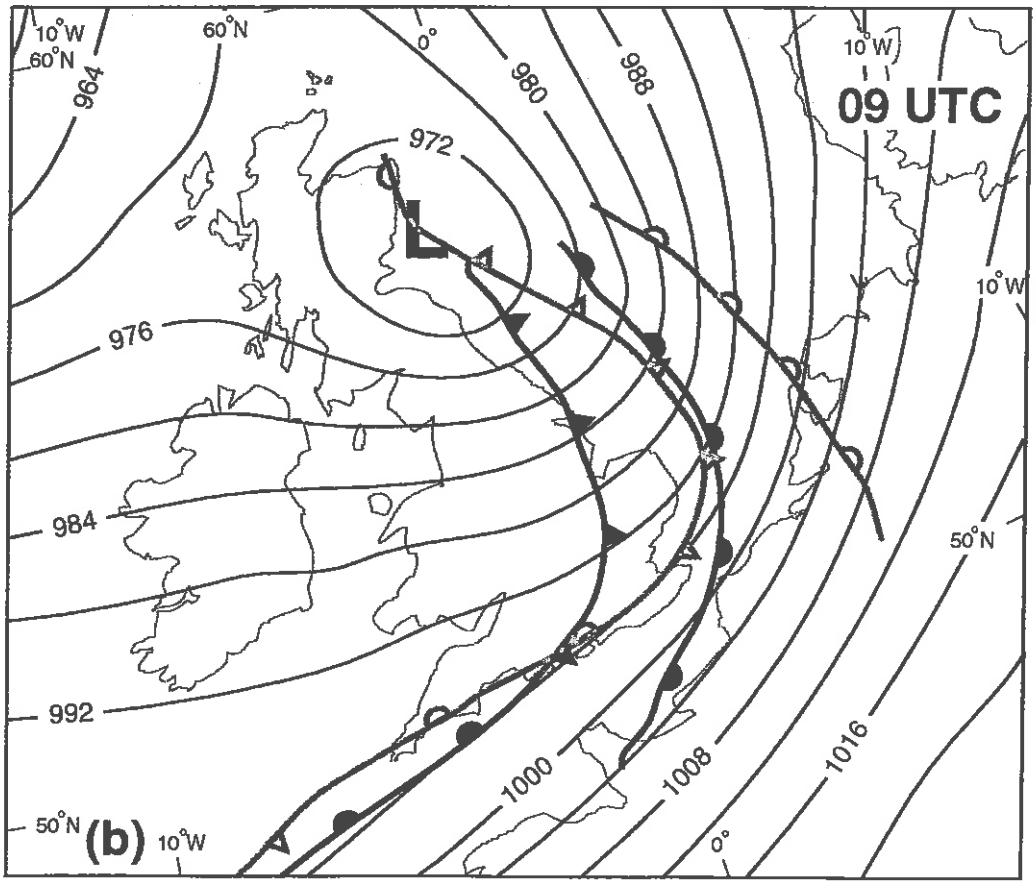
10°W
60°N
60°N
964
0°
980
988
10°W
09 UTC
972
L
976
10°W
984
50°N
992
1000
1008
1016
50°N
(b)
10°W
0°

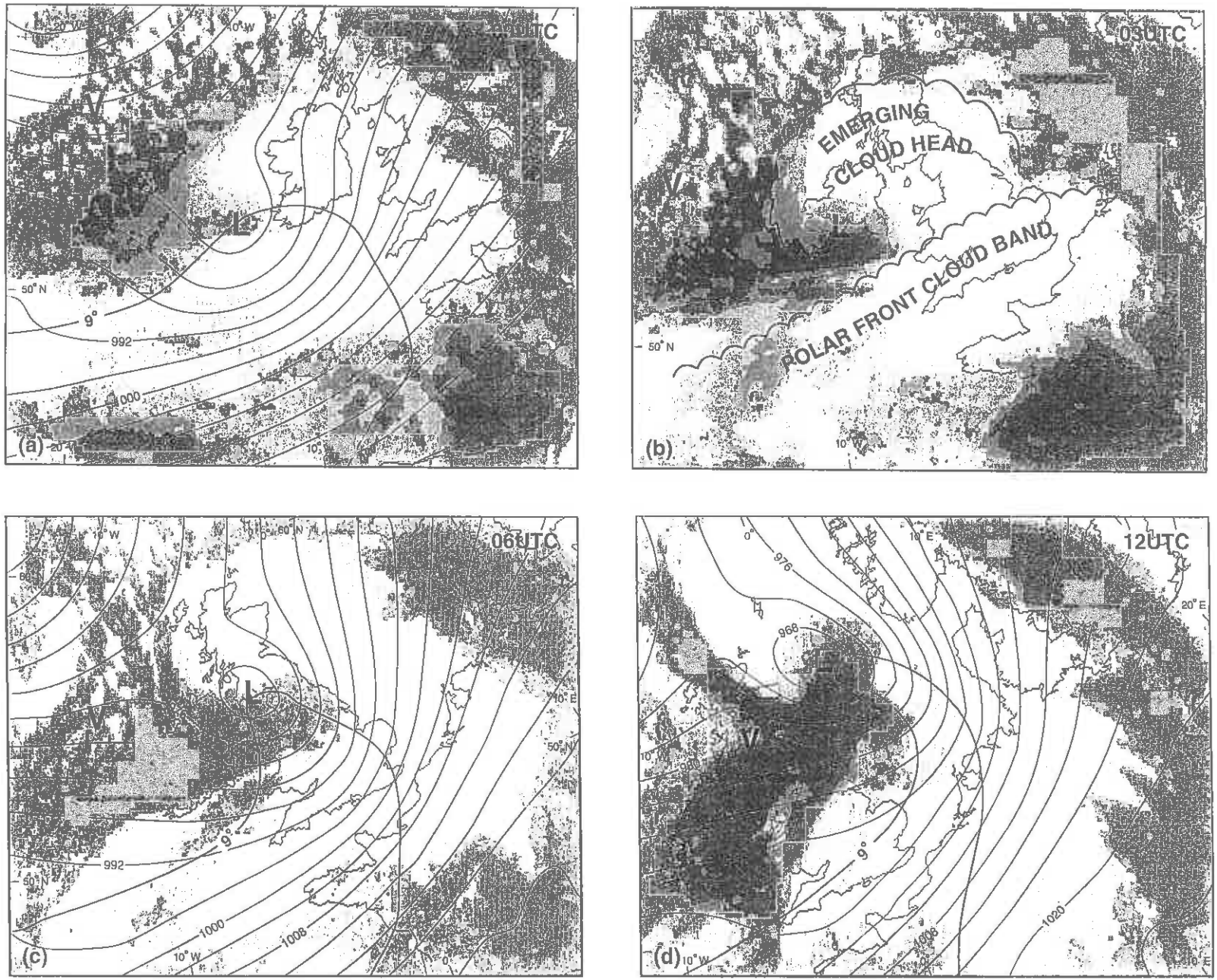

(a)
(b)
(c)
(d)
03UTC
06UTC
12UTC
EMERGING CLOUD HEAD
POLAR FRONT CLOUD BAND
50° N
10° W
20° E
10° E
9°
992
1000
1008
976
968
1020

Figure 3

Figure 4

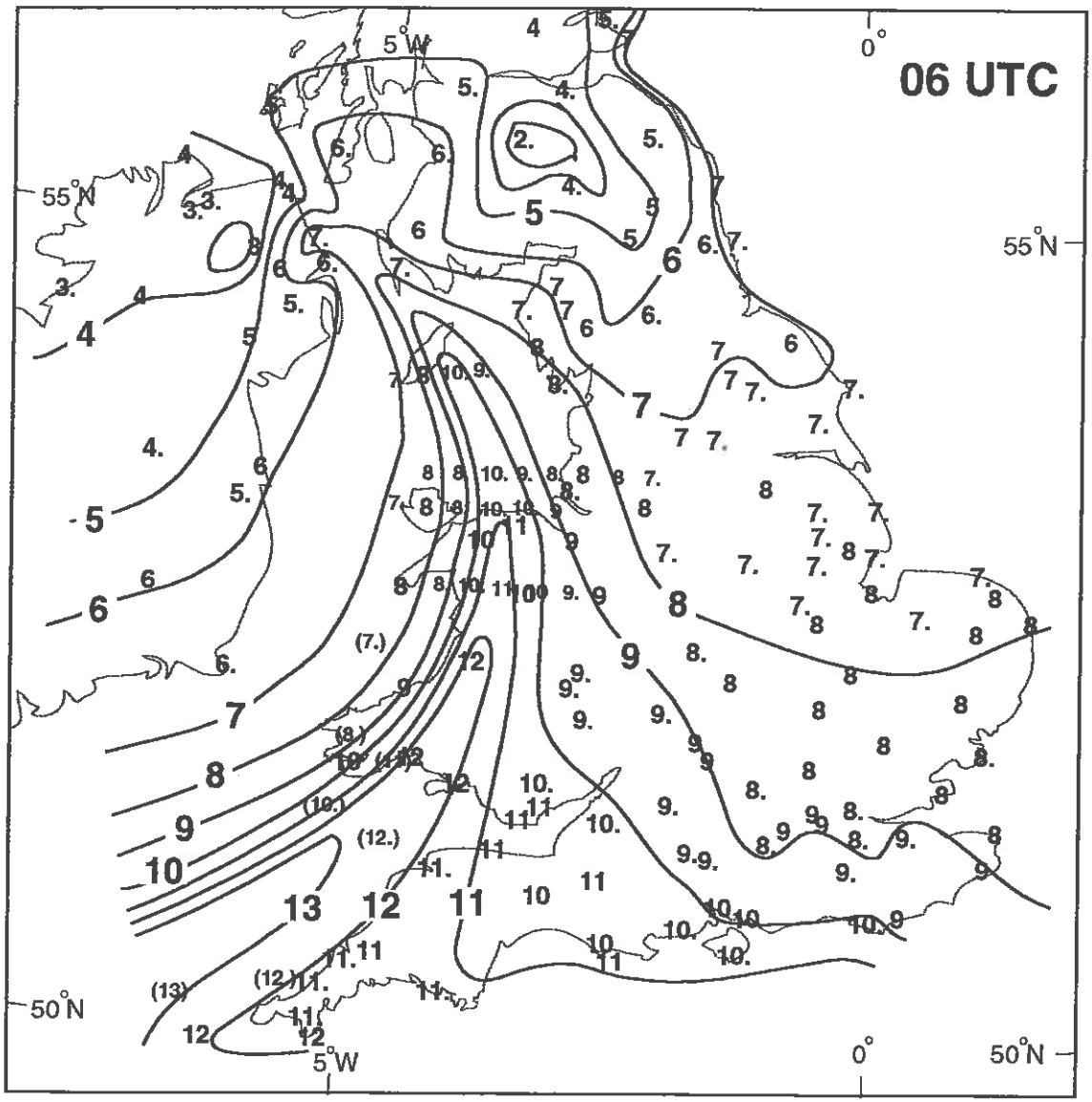

Figure 5

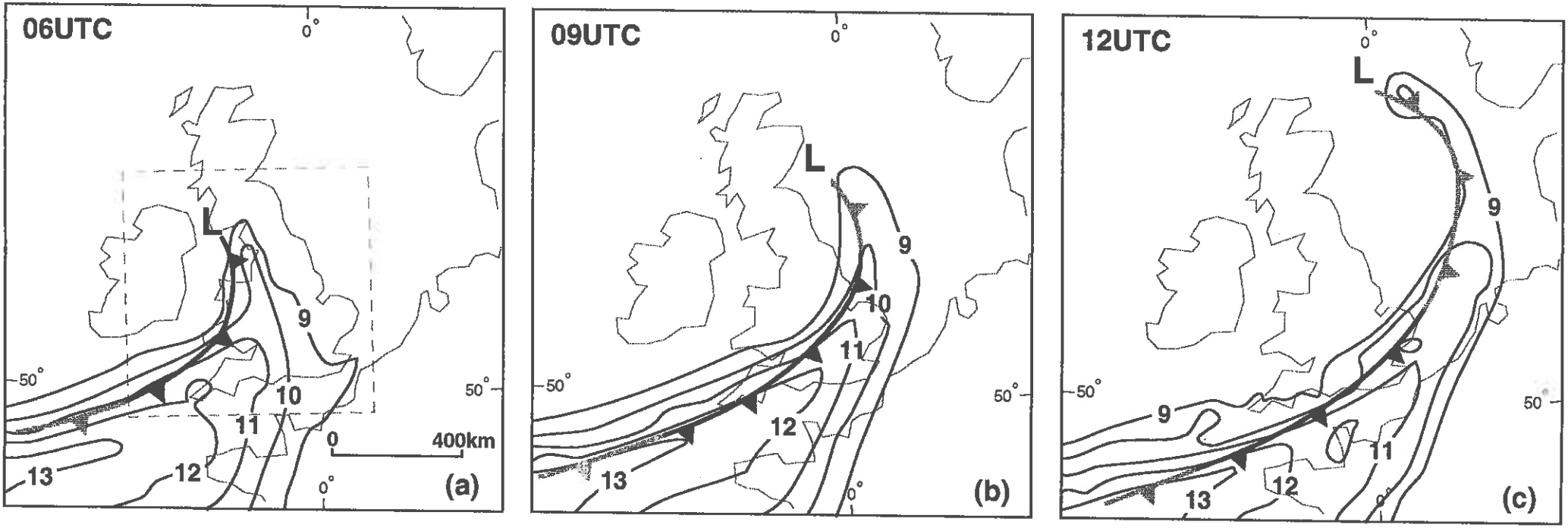
06UTC
0°
L
9
10
11
12
13
50°
50°
0
400km
0°
(a)
09UTC
0°
L
9
10
11
12
13
50°
50°
0°
(b)
12UTC
0°
L
9
9
11
12
13
50°
50
(c)

Figure 6

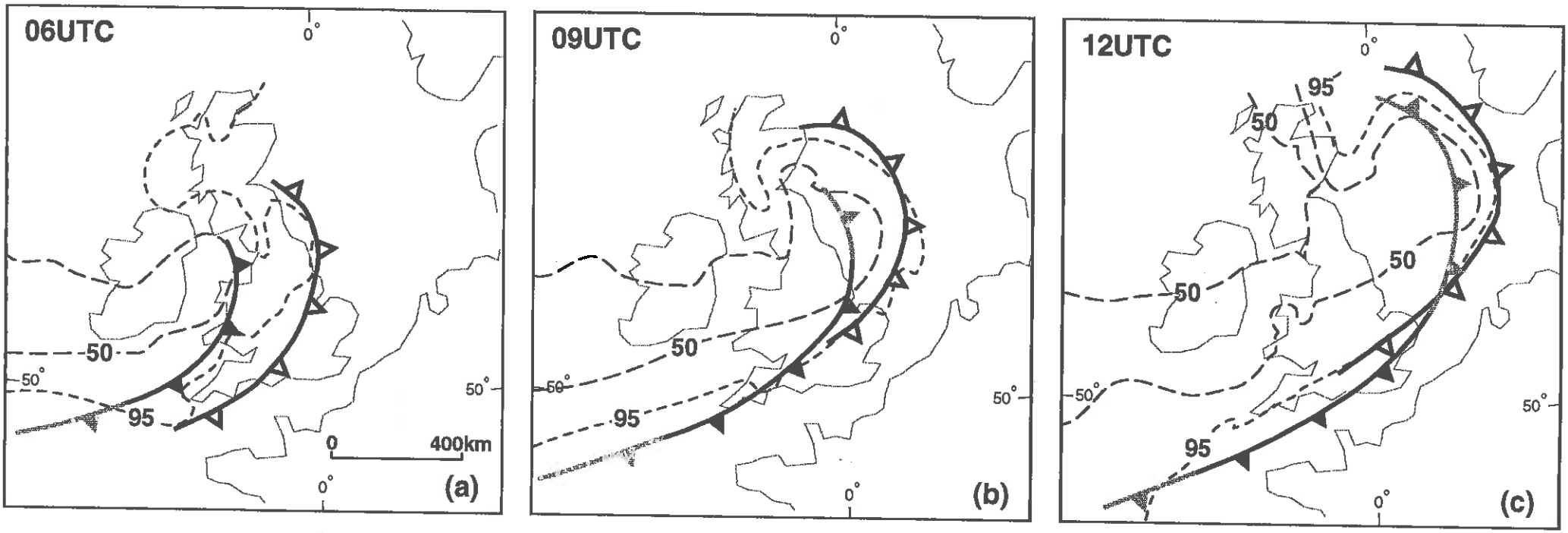
06UTC
0°
50
50°
95
50°
0
400km
0°
(a)
09UTC
0°
50
50°
95
50°
0°
(b)
12UTC
0°
95
50
50
50
50°
95
50°
0°
(c)

Figure 7

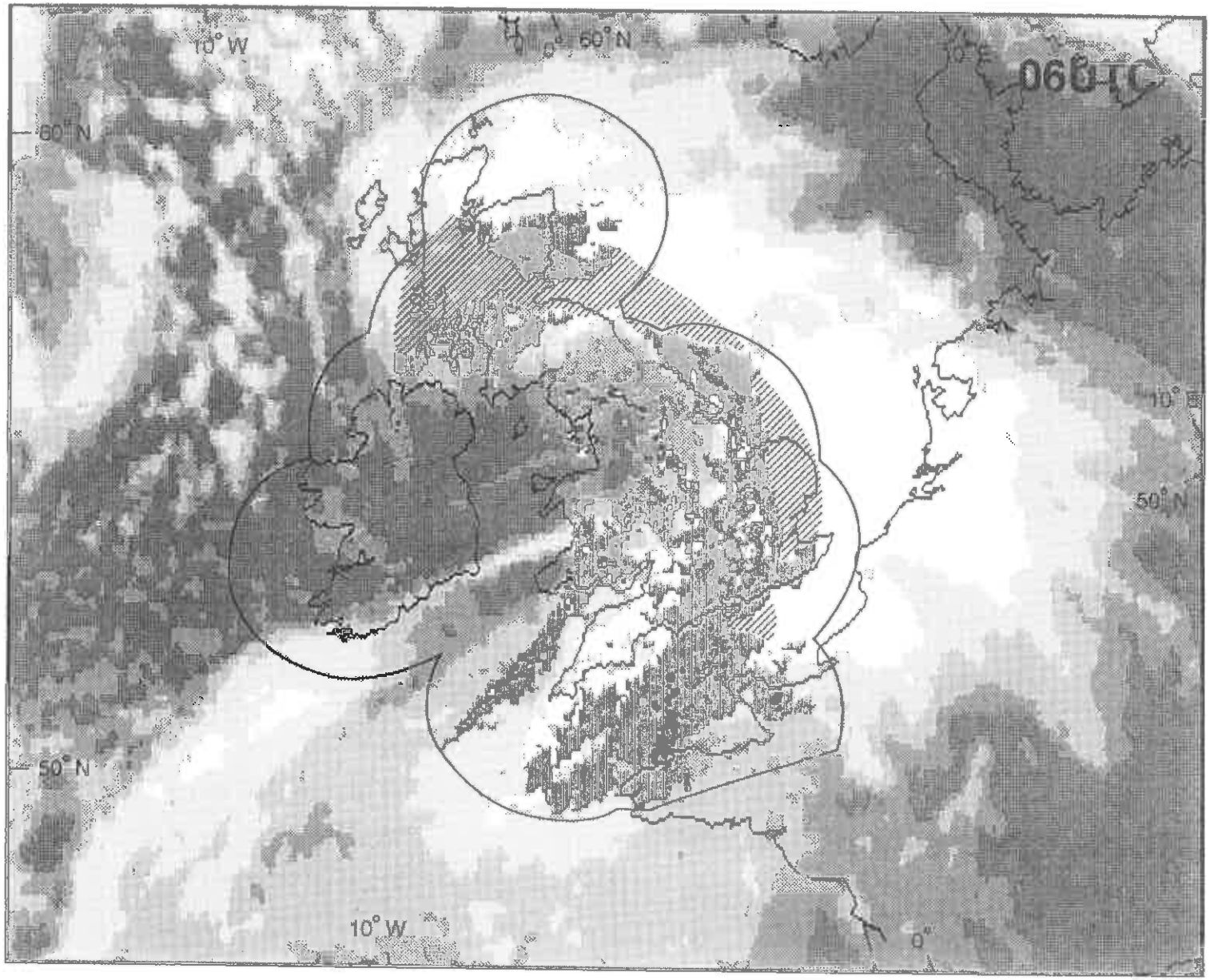

Figure 8

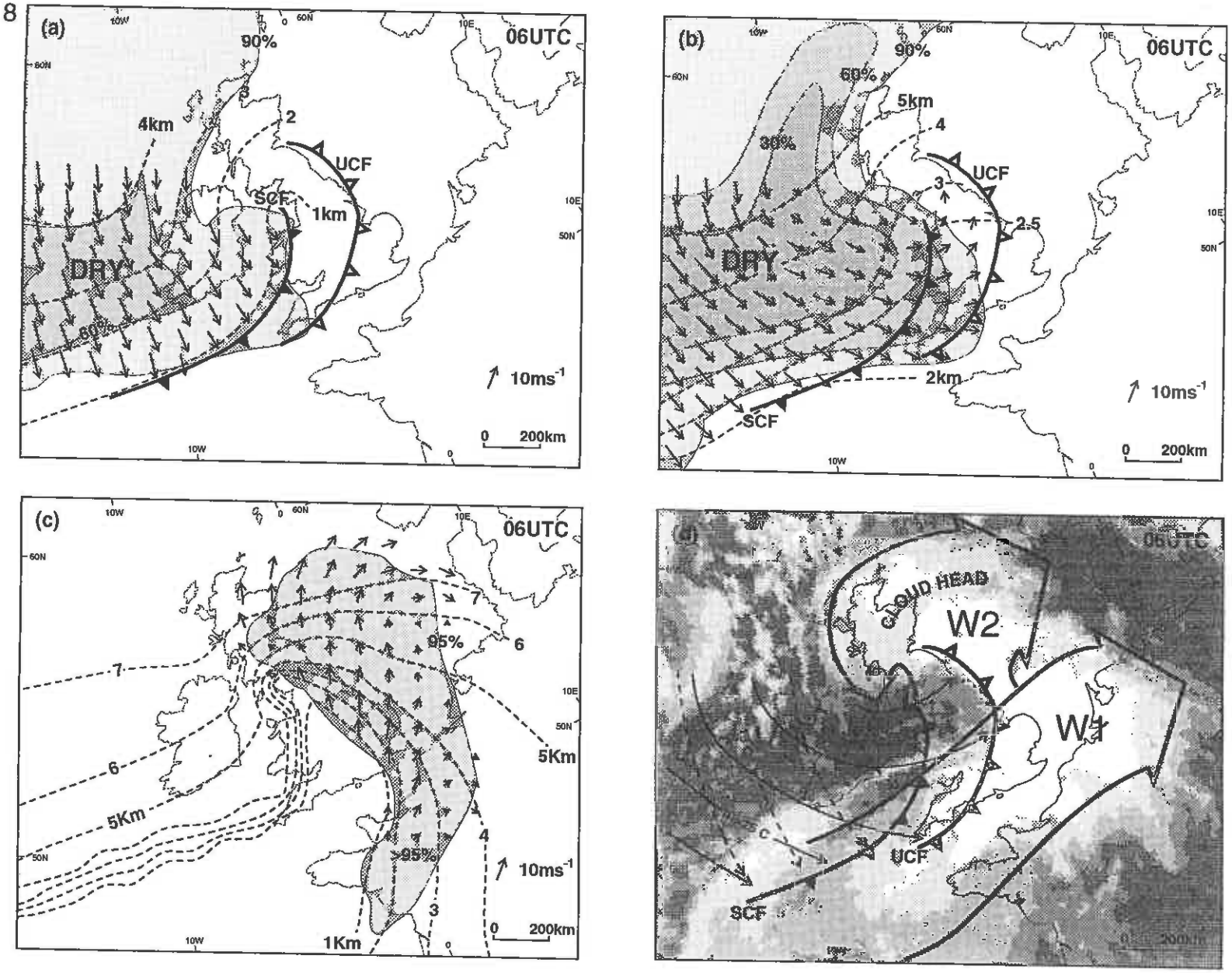
(a)
06UTC
90%
4km
2
UCF
SCF
1km
DRY
60%
10ms-1
0 200km
(b)
06UTC
90%
60%
30%
5km
4
UCF
3
2.5
DRY
2km
SCF
10ms-1
0 200km
(c)
06UTC
7
95%
6
5Km
7
6
5Km
95%
4
10ms-1
3
1Km
0 200km
(d)
06UTC
CLOUD HEAD
W2
W1
UCF
SCF

Figure 9

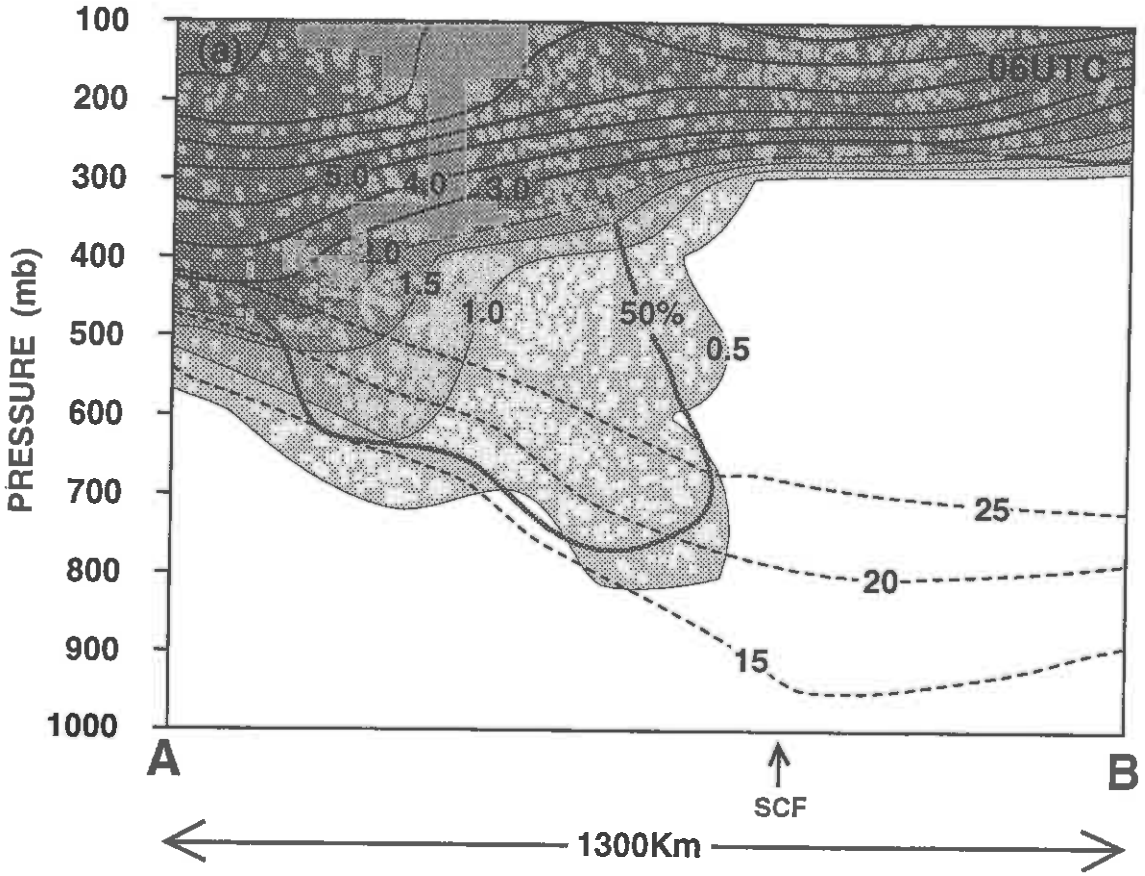
(a)
06UTC
PRESSURE (mb)
100
200
300
400
500
600
700
800
900
1000
5.0
4.0
3.0
2.0
1.5
1.0
50%
0.5
25
20
15
A
B
SCF
1300Km

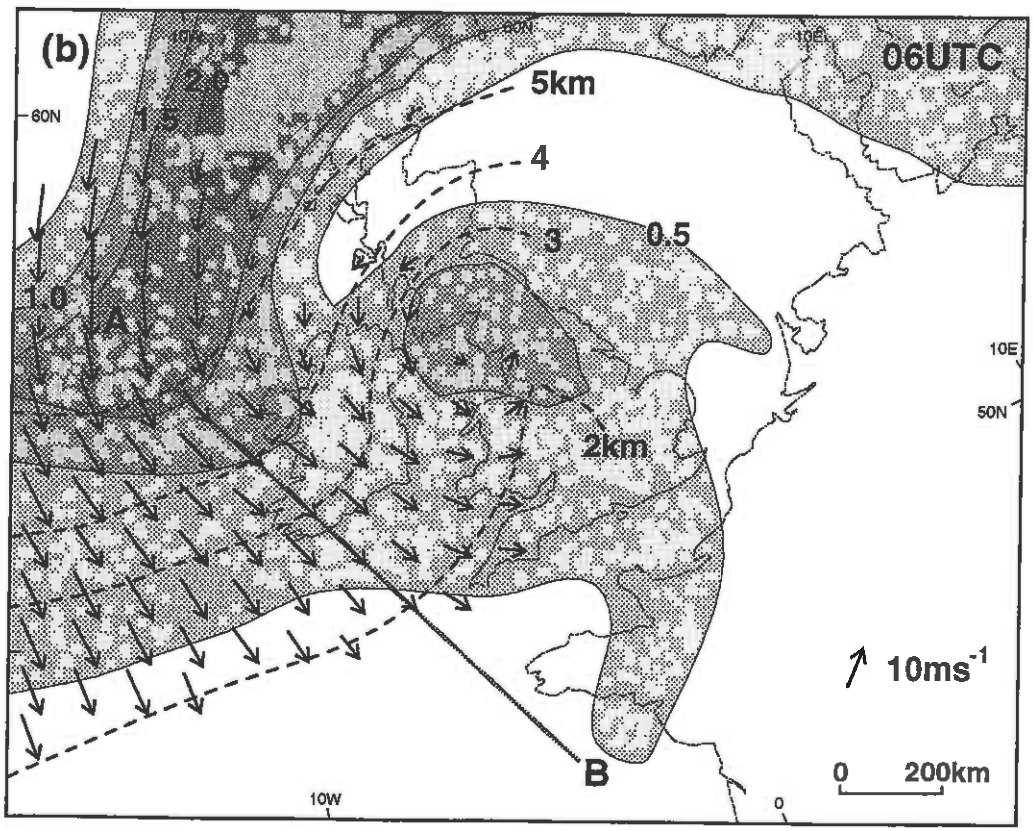
(b)
06UTC
60N
10E
50N
10W
2.0
1.5
1.0
A
B
5km
4
3
0.5
2km
10ms-1
0
200km

Figure 10

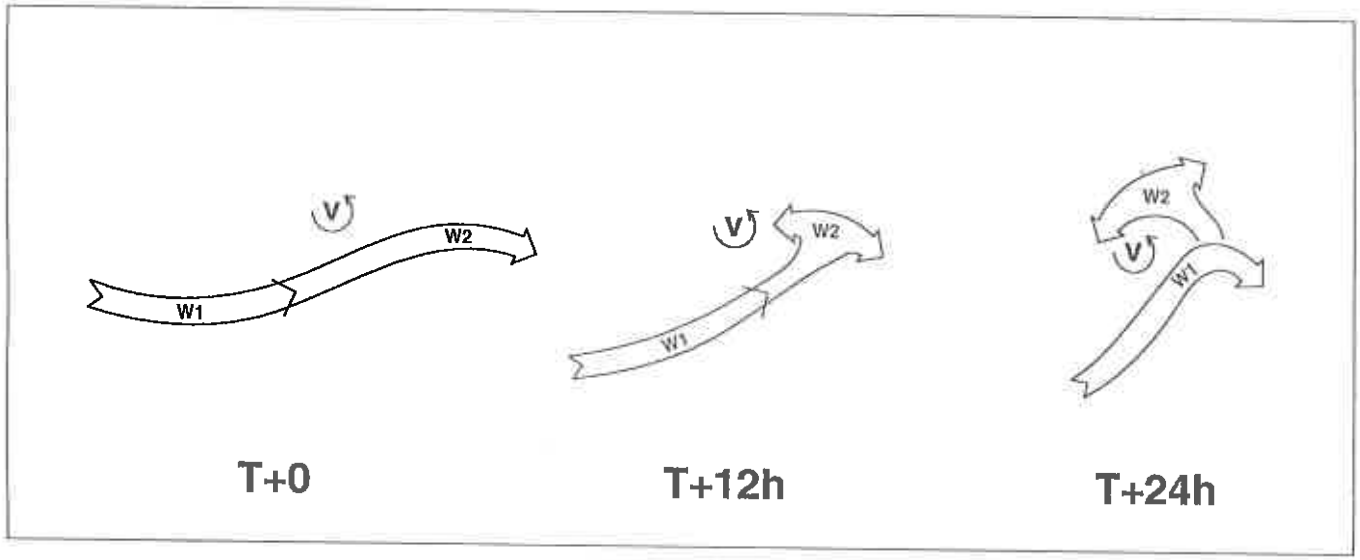

Figure 11

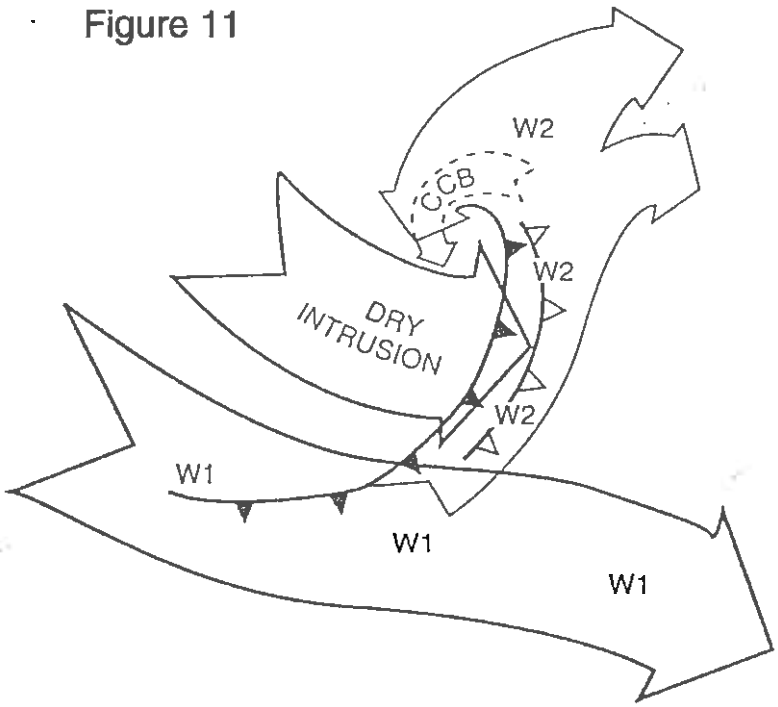

Figure 12

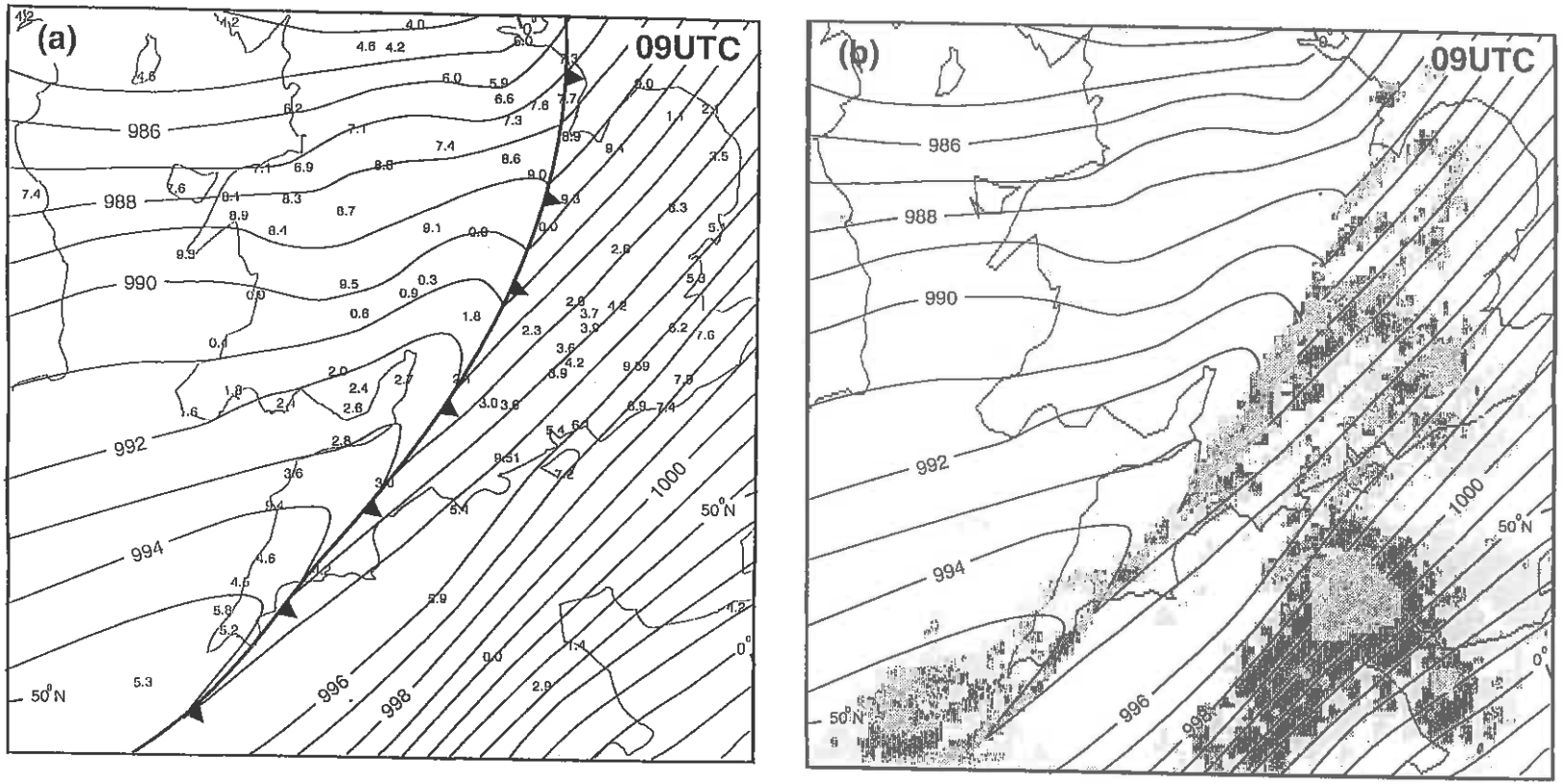
(a)
09UTC
986
988
990
992
994
996
998
1000
50°N
0°
(b)
09UTC
986
988
990
992
994
996
998
1000
50°N
0°

Figure 13

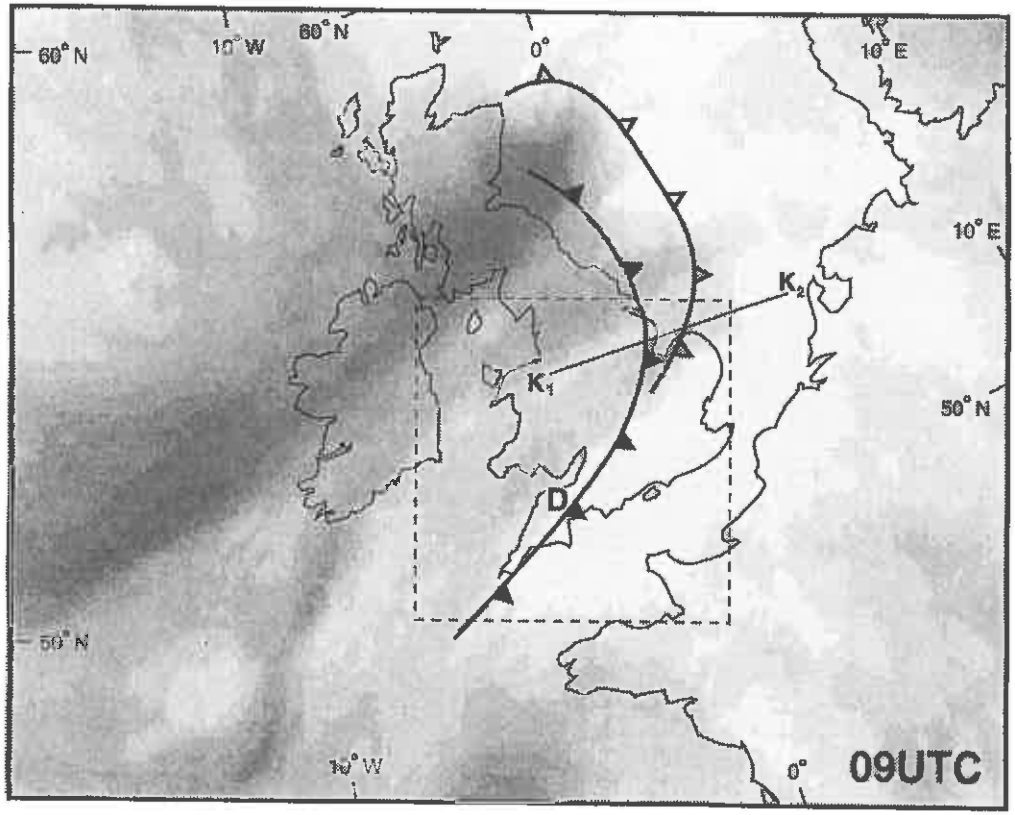

Figure 14

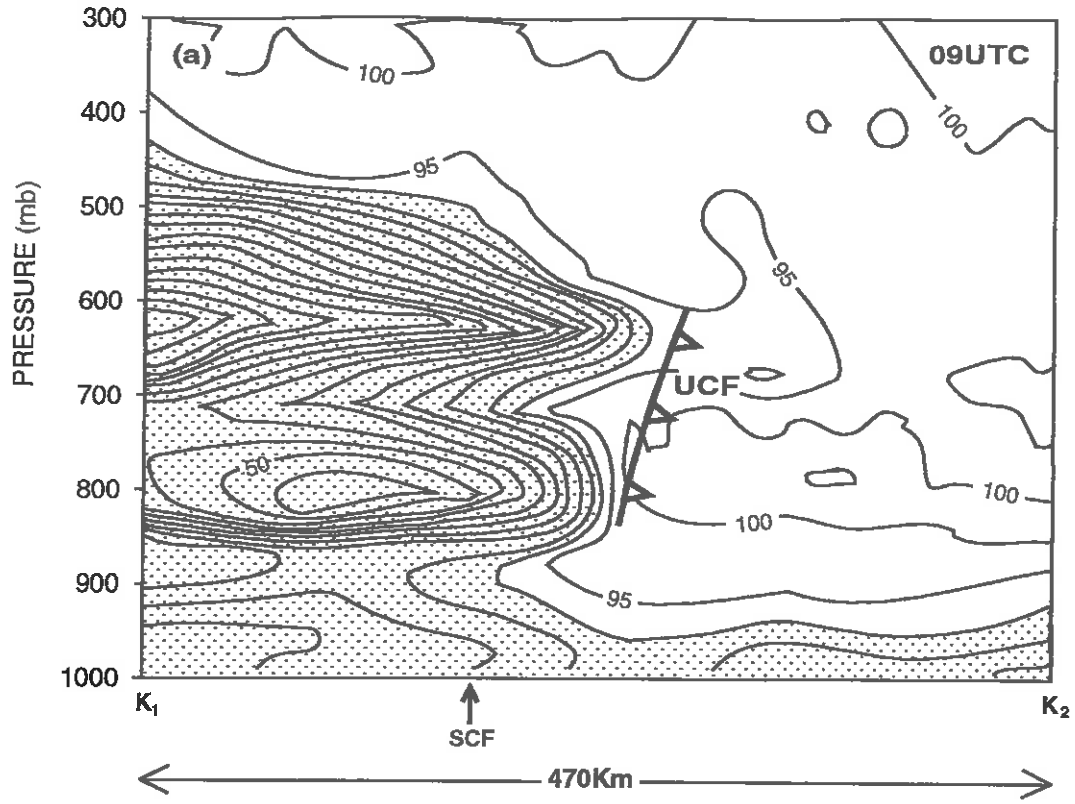
(a)
09UTC
PRESSURE (mb)
300
400
500
600
700
800
900
1000
100
95
50
UCF
K1
K2
SCF
470Km

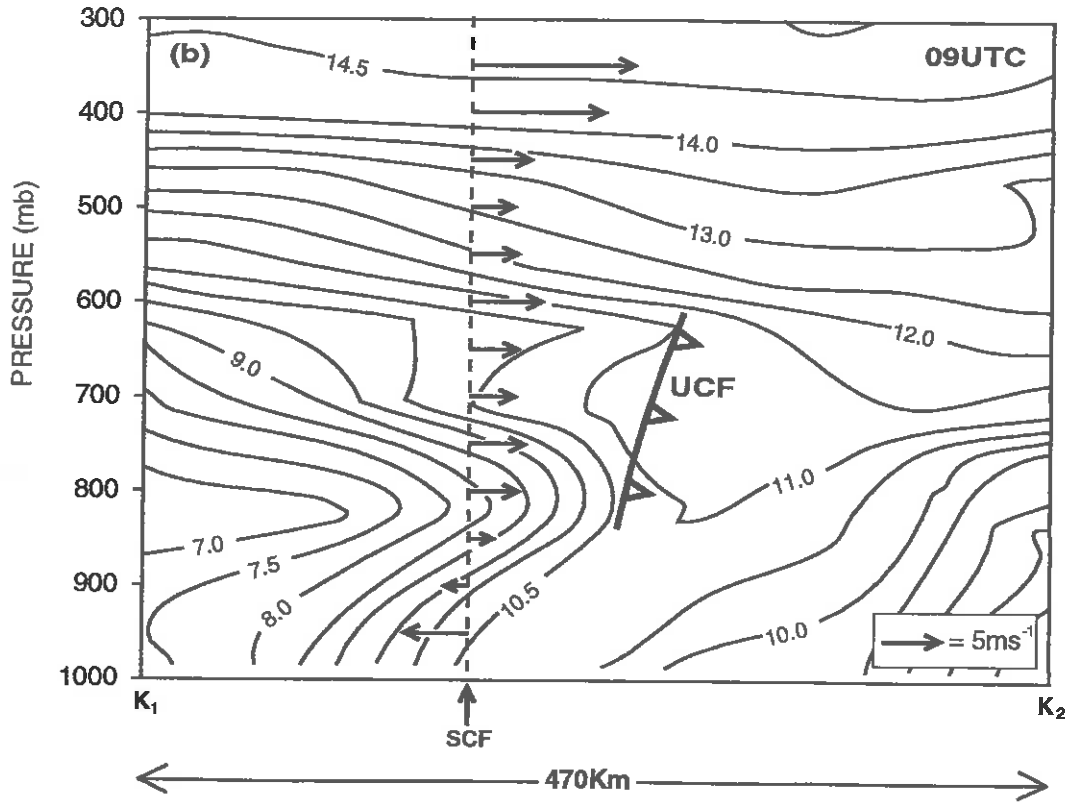
(b)
09UTC
PRESSURE (mb)
300
400
500
600
700
800
900
1000
14.5
14.0
13.0
12.0
11.0
10.0
9.0
7.0
7.5
8.0
10.5
UCF
= 5ms-1
K1
K2
SCF
470Km

Figure 15

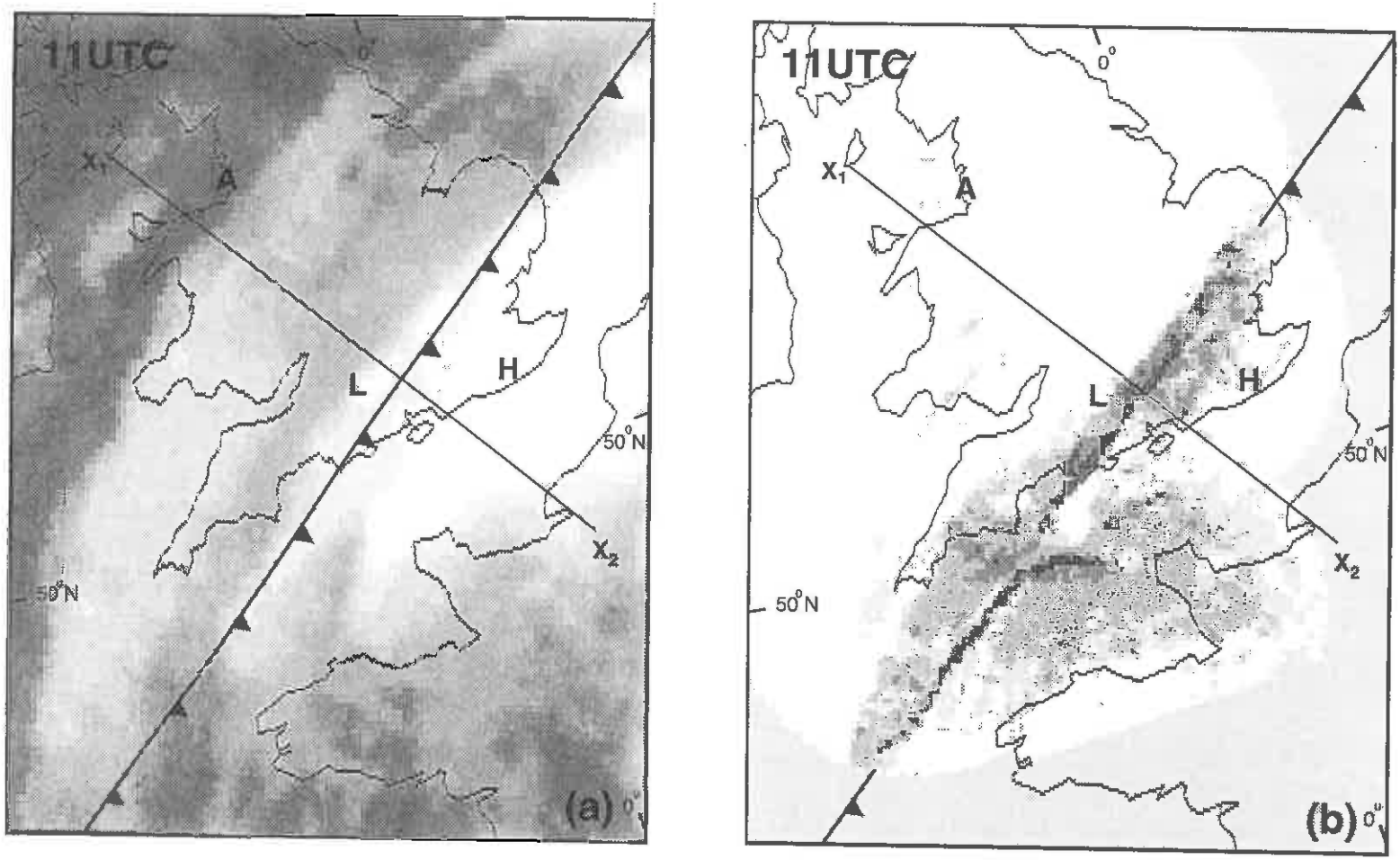

Figure 16

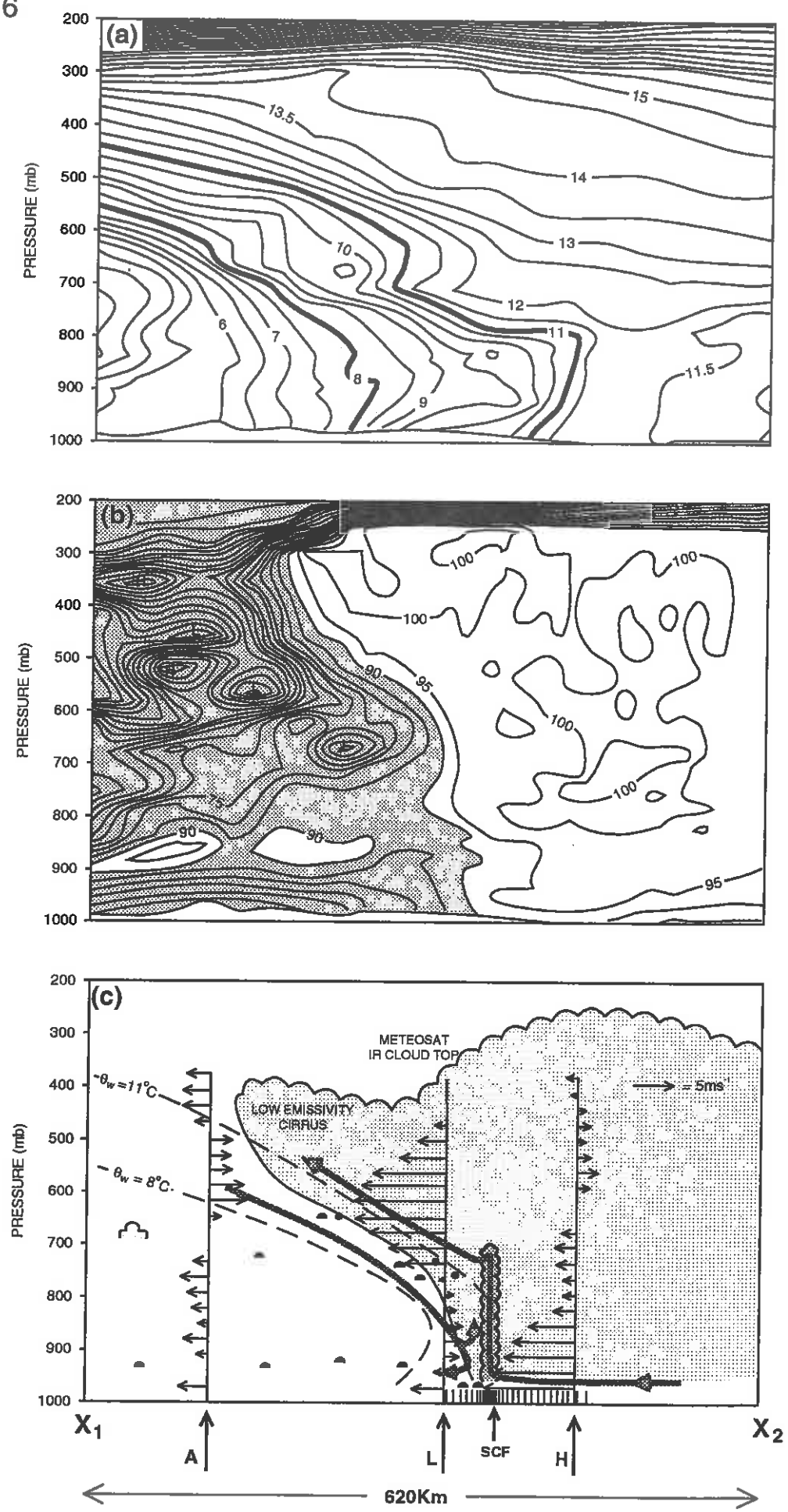
(a)
PRESSURE (mb)
200
300
400
500
600
700
800
900
1000
15
13.5
14
13
10
12
6
7
11
8
11.5
9
(b)
PRESSURE (mb)
100
100
100
90
95
100
100
75
90
90
95
(c)
PRESSURE (mb)
METEOSAT
IR CLOUD TOP
= 5ms⁻¹
LOW EMISSIVITY
CIRRUS
$\theta_w = 11°C$
$\theta_w = 8°C$
X_1
X_2
A
L
SCF
H
620Km

(a)

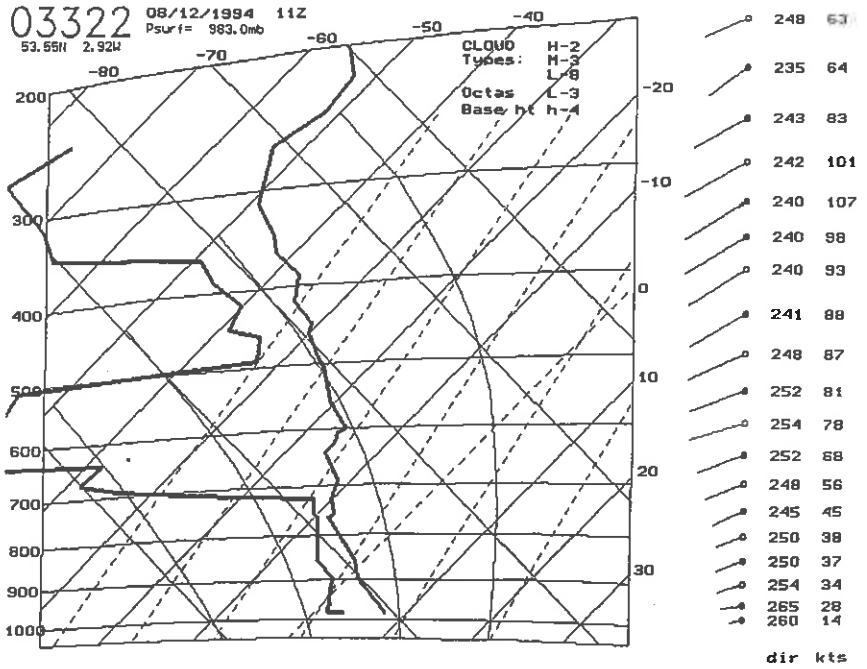

Figure 17

(b)

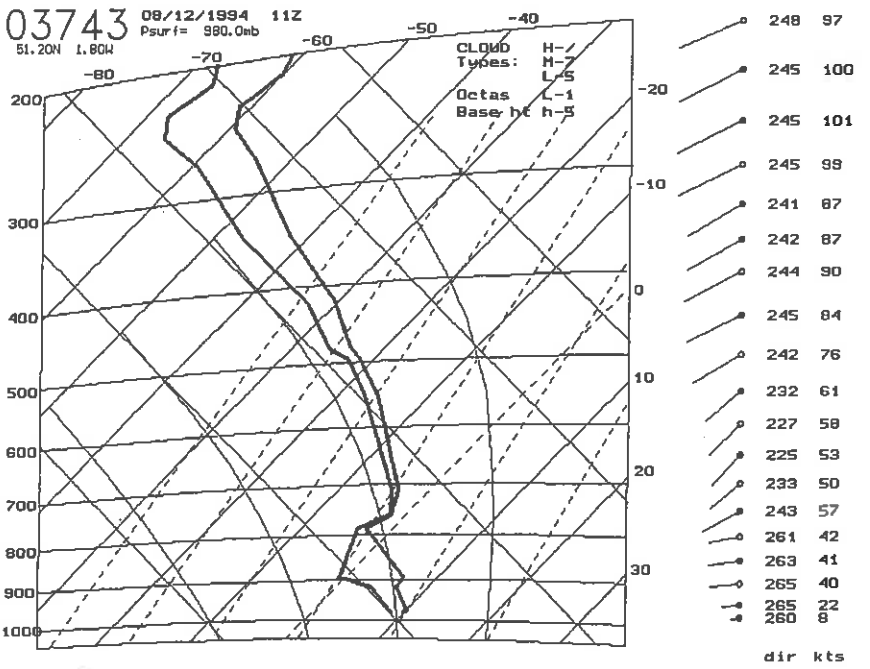

(c)

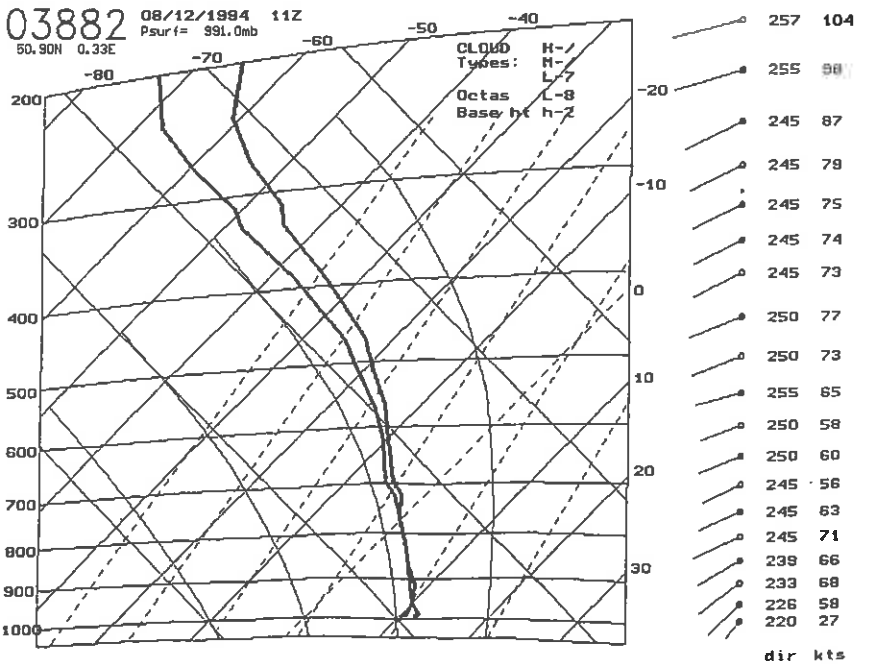

Figure 18

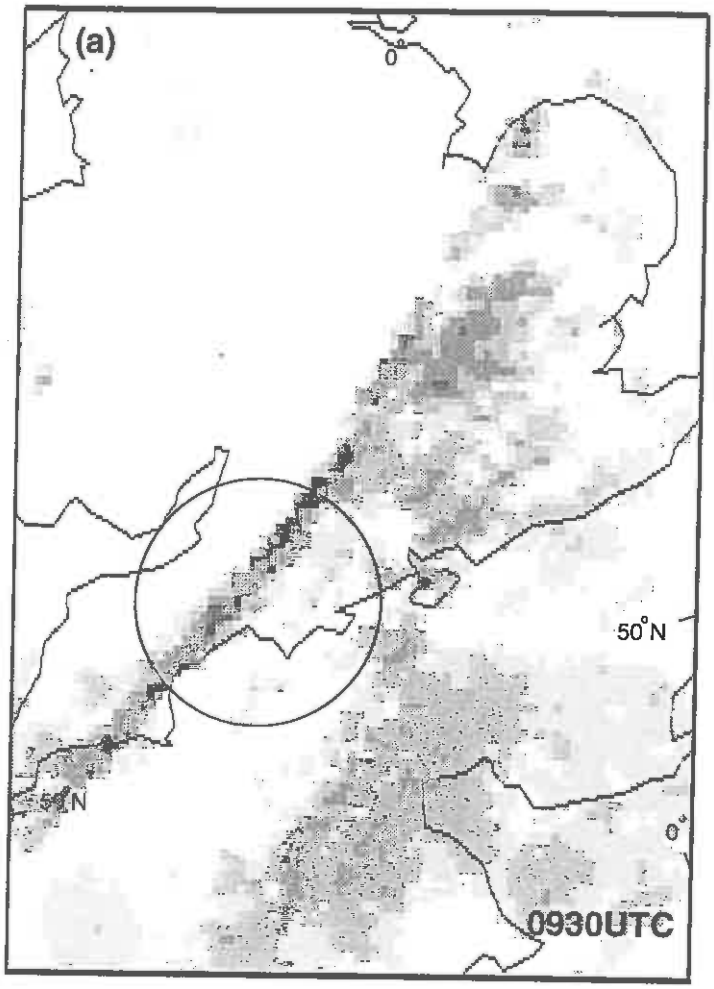

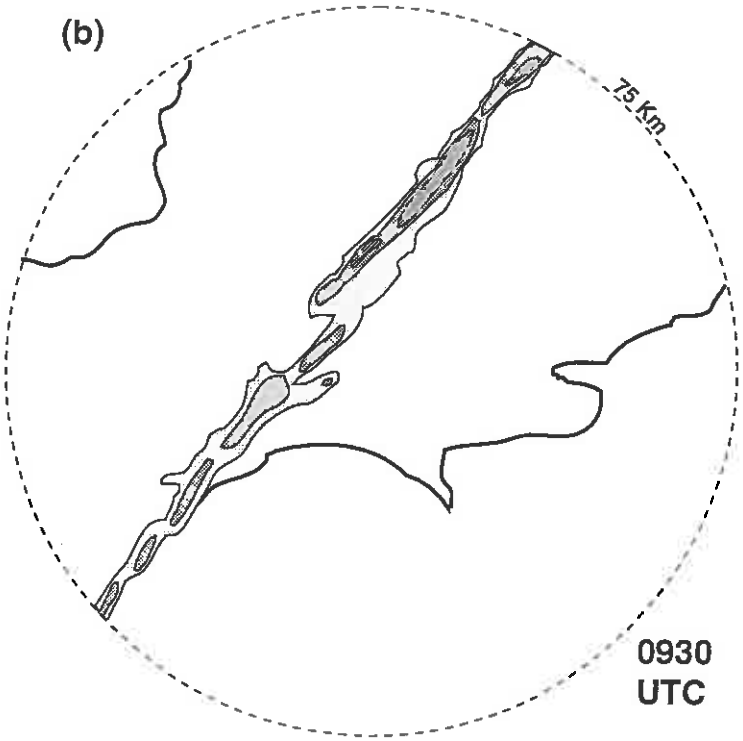

Figure 19

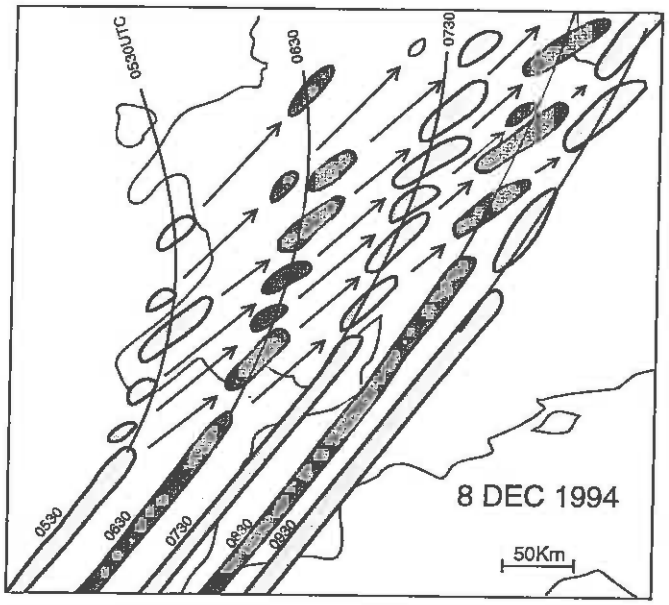

Figure 20

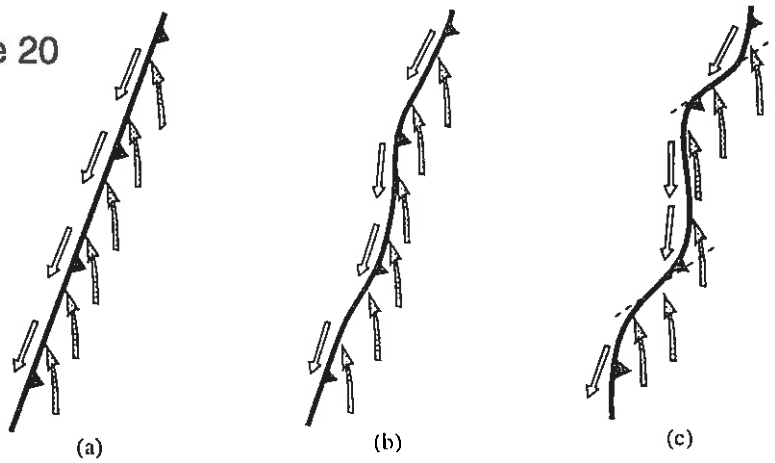

Figure 21

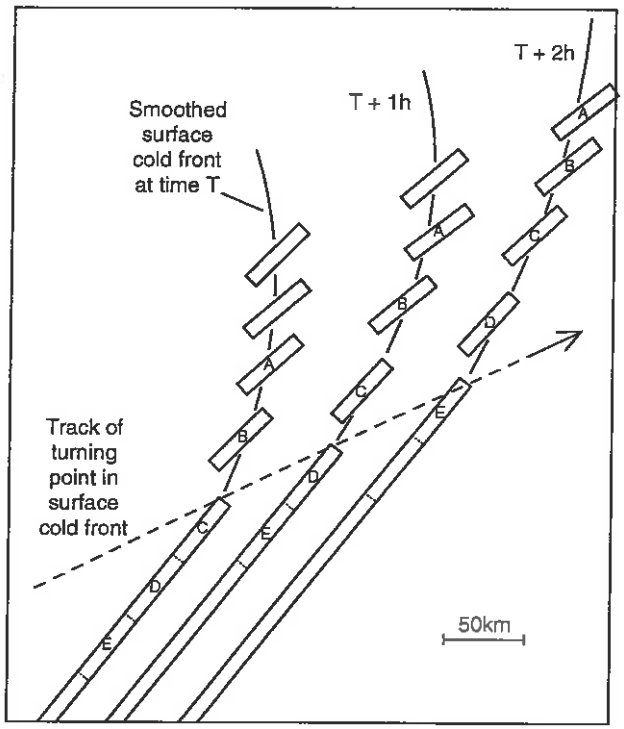

CURRENT JCMM INTERNAL REPORTS

This series of JCMM Internal Reports, initiated in 1993, contains unpublished reports and also versions of articles submitted for publication. The complete set of Internal Reports is available from the National Meteorology Library on loan, if required.

1. **Research Strategy and Programme.**
   K A Browning et al
   January 1993

2. **The GEWEX Cloud System Study (GCSS).**
   GEWEX Cloud System Science Team
   January 1993

3. **Evolution of a mesoscale upper tropospheric vorticity maximum and comma cloud from a cloud-free two-dimensional potential vorticity anomaly.**
   K A Browning
   January 1993

4. **The Global Energy and Water Cycle**
   K A Browning
   July 1993

5. **Structure of a midlatitude cyclone before occlusion.**
   K A Browning and N Roberts
   July 1993

6. **Developments in Systems and Tools for Weather Forecasting.**
   K A Browning and G Szejwach
   July 1993

7. **Diagnostic study of a narrow cold frontal rainband and severe winds associated with a stratospheric intrusion.**
   K A Browning and R Reynolds
   August 1993

8. **Survey of perceived priority issues in the parametrizations of cloud-related processes in GCMs.**
   K A Browning
   September 1993

9. **The Effect of Rain on Longwave Radiation.**
   I Dharssi
   September 1993

10. **Cloud Microphysical Processes - A Description of the Parametrization used in the Large Eddy Model.**
H Swann
July 1994

11. **An Appreciation of the Meteorological Research of Ernst Kleinschmidt.**
A J Thorpe
May 1992

12. **Potential Vorticity of Flow Along the Alps.**
A J Thorpe, H Volkert and Dietrich Heimann
August 1992

13. **The Representation of Fronts.**
A J Thorpe
January 1993

14. **A Parametrization Scheme for Symmetric Instability: Tests for an Idealised Flow.**
C S Chan and A J Thorpe
February 1993

15. **The Fronts 92 Experiment: a Quicklook Atlas.**
Edited by T D Hewson
November 1993

16. **Frontal wave stability during moist deformation frontogenesis. Part 1. Linear wave dynamics**
C H Bishop and A J Thorpe
May 1993

17. **Frontal wave stability during moist deformation frontogenesis. Part 2. The suppression of non-linear wave development.**
C H Bishop and A J Thorpe
May 1993

18. **Gravity waves in sheared ducts.**
S Monserrat and A J Thorpe
October 1993

19. **Potential Vorticity and the Electrostatics Analogy: Quasi-Geostrophic Theory.**
C Bishop and A J Thorpe
November 1993

20. **Recent Advances in the Measurement of Precipitation by Radar.**
A J Illingworth
April 1993

21. **Micro-Physique et Givrage. Cloud Microphysics and Aircraft Icing.**
A J Illingworth
May 1993

22. **Differential Phase Measurements of Precipitation.**
M Blackman and A J Illingworth
May 1993

23. **Estimation of Effective Radius of Cloud Particles from the Radar Reflectivity.**
N I Fox and A J Illingworth
May 1993

24. **A Simple Method of Dopplerising a Pulsed Magnetron Radar.**
L Hua, A J Illingworth and J Eastment
November 1993

25. **Radiation and Polar Lows.**
George C Craig
February 1994

26. **Collected preprints submitted to International Symposium on the Life Cycles of Extratropical Cyclones; Bergen, Norway, 27 June - 1 July 1994**
April 1994

27. **Convective Frontogenesis**
Douglas J Parker and Alan J Thorpe
April 1994

28. **Improved Measurement Of The Ice Water Content In Cirrus Using A Total Water Evaporator**
Philip R A Brown and Peter N Francis
April 1994

29. **Mesoscale Effects of a Dry Intrusion within a Vigorous Cyclone**
K A Browning and B W Golding
April 1994

30. **GEWEX Cloud System Study, Science Plan**
May 1994

31. **Parametrization of Momentum Transport by Convectively Generated Gravity Waves**
R Kershaw
February 1995

32. **Mesoscale Modelling Newsletter, No. 5**
May 1994

33. **Observations of the mesoscale sub-structure in the cold air of a developing frontal cyclone**
K A Browning, S A Clough, C S A Davitt, N M Roberts and T D Hewson
May 1994

34. **Longwave Radiative Forcing of a Simulated Tropical Squall Line**
Imtiaz Dharssi
July 1994

35. **On the nature of the convective circulations at a kata-cold front**
K A Browning
September 1994

36. **Collected preprints of papers submitted to the COST-75 International Seminar on Advanced Weather Radar Systems, Brussels, 20-23 September 1994**
November 1994

37. **Use of satellite imagery to diagnose events leading to frontal thunderstorms: Parts I and II of a case study**
K A Browning and N M Roberts
November 1994

38. **The role of spaceborne millimetre-wave radar in the global monitoring of ice cloud**
P R A Brown, A J Illingworth, A J Heymsfield, G M McFarquhar, K A Browning and M Gosset
December 1994

39. **Potential Vorticity Inversion**
Michal Ziemianski
October 1994

40. **Theory of mature tropical cyclones; A comparison between Kleinschmidt (1951) and Emanual (1986)**
Suzanne L Gray
December 1994

41. **Dispersion and removal of pollutants during the passage of an atmospheric frontal system**
N R Gimson
December 1994

42. **The role of snow sublimation in frontogenesis**
D J Parker and A J Thorpe
December 1994

43. **Potential vorticity and the electrostatics Analogy: Ertel-Rossby formulation**
A J Thorpe and C H Bishop
December 1994

44. **Mesoscale aspects of extratropical cyclones: an observational perspective**
K A Browning
January 1995

45. **A Polar Low Outbreak: Evolution and Mesoscale Structures**
T D Hewson, G C Craig and C Claud
February 1995

46. **Generation of near-surface gusts by deep convection**
K Nakamura and R Kershaw
April 1995

47. **Attribution concepts applied to the omega equation**
S A Clough, C S A Davitt and A J Thorpe
June 1995

48 **Parametrization of mixed-phase cloud and precipitation**
Susan P Ballard and M Gerard Hutchinson
June 1995

49 **Short-range forecasting of stratocumulus: Initialization V Prediction**
Susan P Ballard, Simon D Jackson and B Macpherson
June 1995

50 **Contributions of the JCMM/Dept of Meteorology Radar Group to the 27th AMS Radar Meteorology Conference, Vail October 1995**
June 1995

51 **Cold pools in shear**
Douglas J Parker
September 1995

52 **High-resolution analysis of frontal fracture**
K A Browning, S P Ballard and C S A Davitt
September 1995

53 **The Albedo of Broken Cloud Fields: Calculations using a modified two stream radiation code**
Imtiaz Dharssi and Roy Kershaw
October 1995

54 **Parametrization of momentum transport by convection. I: Theory and cloud modelling results**
R Kershaw and D Gregory
November 1995

55 **Variation of frontal structure along a cold front**
K A Browning and N M Roberts
November 1995

Met Office Joint Centre for Mesoscale Meteorology Department of Meteorology
University of Reading PO Box 243 Reading RG6 6BB United Kingdom
Tel: +44 (0)118 931 8425 Fax: +44 (0)118 931 8791
www.metoffice.com